Density ratio effects on reacting bluff-body flow field characteristics

Benjamin Emerson[1]†, **Jacqueline O'Connor**[1]‡, **Matthew Juniper**[2]
and Tim Lieuwen[1]

[1] Georgia Institute of Technology, School of Aerospace Engineering, 270 Ferst Dr, Atlanta, GA 30332, USA

[2] Cambridge University Engineering Department, Trumpington Street, Cambridge CB2 1PZ, UK

The wake characteristics of bluff-body-stabilized flames are a strong function of the density ratio across the flame and the relative offset between the flame and shear layer. This paper describes systematic experimental measurements and stability calculations of the dependence of the flow field characteristics and flame sheet dynamics upon flame density ratio, ρ_u/ρ_b, over the Reynolds number range of 1000–3300. We show that two fundamentally different flame/flow behaviours are observed at high and low ρ_u/ρ_b values: a stable, noise-driven fixed point and limit-cycle oscillations, respectively. These results are interpreted as a transition from convective to global instability and are captured well by stability calculations that used the measured velocity and density profiles as inputs. However, in this high-Reynolds-number flow, the measurements show that no abrupt bifurcation in flow/flame behaviour occurs at a given ρ_u/ρ_b value. Rather, the flow field is highly intermittent in a transitional ρ_u/ρ_b range, with the relative fraction of the two different flow/flame behaviours monotonically varying with ρ_u/ρ_b. This intermittent behaviour is a result of parametric excitation of the global mode growth rate in the vicinity of a supercritical Hopf bifurcation. It is shown that this parametric excitation is due to random fluctuations in relative locations of the flame and shear layer.

Key words: absolute/convective instability, combustion, wakes

1. Background

The unsteady flow fields in reacting bluff-body flows are often dominated by large-scale coherent structures, embedded in a background of acoustic waves and broadband fine-scale turbulence. These large-scale structures play important roles in such processes as combustion instabilities (Smith & Zukoski 1985; Crump *et al.* 1986; Yang & Culick 1986; Poinsot *et al.* 1987; Soteriou & Ghoniem 1994), mixing and entrainment, flashback, and blowoff (Shanbhogue, Husain & Lieuwen 2009*a*). These structures arise because of underlying hydrodynamic instabilities of the flow field (Criminale, Jackson & Joslin 2003). The objective of this study is to characterize the effects of the flame upon the absolute and convective instability characteristics

† Email address for correspondence: bemerson@gatech.edu

‡ Present address: Sandia National Laboratories, Engine Combustion Department, PO Box 969 MS 9053, Livermore, CA 94551-0969, USA.

of the flow (Huerre & Monkewitz 1990; Anderson, Hertzberg & Mahalingam 1996; Godreche & Manneville, 1998; Schmid & Henningson, 2001).

There are two key flow features downstream of the bluff body in high-Reynolds-number flows; these are the separating free shear layers (Cardell 1993) and the wake, both of which strongly influence the flame. The separated shear layer is *convectively* unstable due to the Kelvin–Helmholtz mechanism for $Re_D > \sim 1200$ (Prasad & Williamson 1997), where Re_D is the Reynolds number based on velocity at the lip (U_{lip}) and bluff-body diameter (D), leading to shear layer rollup into tightly concentrated vorticity. In most practical configurations, the flame lies nearly parallel to the flow and, thus, almost directly in the bluff-body shear layer for high-velocity flows. Small perturbations in convectively unstable flows are amplified as they convect downstream, but not locally at their source locations. In other words, convectively unstable flows have positive growth rates for some disturbance wavelengths with non-zero group velocity, but all disturbances of zero group velocity are damped. These flows are disturbance amplifiers (Briggs 1964; Bers 1983; Huerre & Monkewitz 1985).

The separating vorticity sheets on both sides of the bluff body roll up, which induces a flow field that wraps the flame around these regions of concentrated vorticity. This wake region may be globally unstable, given the presence of a large enough pocket of absolute instability. The key distinction from the convectively unstable flow is that absolutely unstable profiles lead to amplification of some disturbances of zero group velocity. Therefore, these flows exhibit intrinsic oscillations at a global mode frequency (Briggs 1964; Bers 1983; Huerre & Monkewitz 1985).

In non-reacting flows, the bluff-body wake is absolutely unstable, and characterized by large-scale, asymmetric rollup of the wake into staggered vortical structures (Perry, Chong & Lim 1982), often referred to as the von Kármán vortex street. This instability has a characteristic frequency of (Prasad & Williamson 1997)

$$f_{BVK} = St_D \frac{U_{lip}}{D} \qquad (1.1)$$

where St_D is the Strouhal number. For circular cylinders, St_D is independent of Reynolds number ($St_D = 0.21$) in the turbulent-shear-layer laminar-boundary-layer regime, $\sim 1000 < Re_D < \sim 200\,000$ (Cantwell & Coles 1983). Above $Re_D \sim 200\,000$, the boundary layer starts to transition to turbulence and there are some indications that this Strouhal number value changes (Roshko 1961; Bearman 1969). Bluff-body shape also influences the Strouhal number for the von Kármán vortex street (Blevins 1977). In particular, St_D is lower for 'bluffer' bodies, i.e. those with higher drag and wider wakes (Roshko 1955). For example, $St_D \sim 0.18$ for a 90° 'v-gutter' and drops to 0.13 for a sharp-edge, vertical flat plate (Huang & Chang 2004). Roshko (1954, 1955) suggests that St_D fundamentally scales with the wake width and, therefore, care must be applied in inferring Strouhal numbers from one bluff-body shape to another. For example, flow separation is retarded for circular bluff bodies when the boundary layer transitions to turbulence, implying a reduction in wake width and turbulent vortex rollup (Zdravkovich 1997). In contrast, the flow separation point does not move in bluff bodies with sharp separation points.

These baseline flow stability characteristics are altered by heating the fluid in the wake (Roshko 1954; Yu & Monkewitz 1990; Cardell 1993; Zdravkovich 1997; Erickson & Soteriou 2011), and through base bleeding/blowing, to name a couple of examples. Of most interest to this study are wake density ratio effects (due to heating, for example). It has been shown that a sufficiently hot wake relative to the free stream eliminates the absolute instability of the wake, so that the flow's dynamics are then
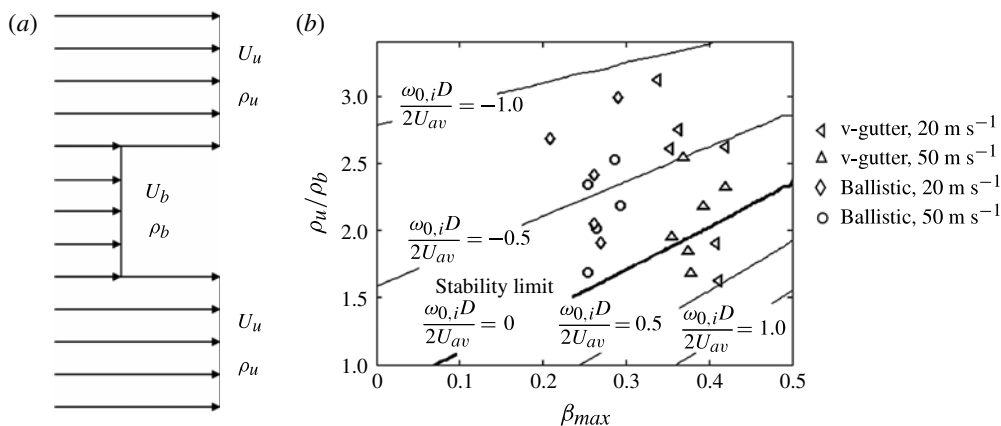
FIGURE 1. (*a*) Flow geometry used for the local parallel stability analysis, and (*b*) tested conditions overlaid onto a stability map obtained from a local parallel stability analysis for the wake's sinuous mode (Yu & Monkewitz 1990).

controlled by the convectively unstable shear layers. For example, Yu & Monkewitz (1990) performed parallel stability analyses of variable-density wakes, characterized by an outer flow with a density, ρ_u, and time-averaged velocity, U_u, and wake region with density ρ_b and velocity U_b (see figure 1). For an inviscid flow with a step jump in properties between the two fluids, they show that the absolute stability boundary depends upon density ratio between the outer flow and the wake, as well as the ratio of reverse flow velocity in the wake to outer flow velocity, β, defined as

$$\beta(x) = -\frac{U_b(x)}{U_u(x)}, \tag{1.2}$$

where subscripts u and b denote unburned and burned respectively.

The convective/absolute stability boundary predicted by their analysis is plotted in figure 1. For the purpose of this study, only the sinuous (asymmetric) mode stability boundary is plotted, as it is more easily destabilized in wakes than the varicose (symmetric) mode. This plot shows that absolute instability is promoted with lower density ratios, ρ_u/ρ_b, and higher wake reverse flow velocities. For the reacting mixtures considered in this study, the density ratios plotted in the figure are also essentially identical to the flame temperature ratio, T_b/T_u. Similar stability calculations have also been performed using more realistic velocity and density ratio profiles, such as hyperbolic tangent profiles, and incorporating viscous effects (Monkewitz 1988).

In the rest of this introduction focus is shifted from the general hydrodynamic stability literature to the more specific reacting-flow literature. A variety of prior studies have noted fundamental differences in the dynamic character of the flame and/or flow field at different velocity and fuel/air ratio conditions (Beer & Chigier 1972; Bill & Tarabanis 1986), particularly under near-blowoff conditions (Thurston 1958; Williams 1966; Yamaguchi, Ohiwa & Hasegawa 1985; Nair & Lieuwen 2005; Kiel *et al.* 2006; Nair 2006; Kiel *et al.* 2007) or in flames utilizing highly preheated reactants (Kiel *et al.* 2006; Cross *et al.* 2010; Erickson & Soteriou 2011). Near blowoff, the flame exhibits substantially increased levels of fluctuations in position, due to local extinction on the flame (Karlovitz *et al.* 1953; Yamaguchi *et al.* 1985; Hertzberg, Shepherd & Talbot 1991; Yang, Yen & Tsai 1994; Kim *et al.* 2006), as
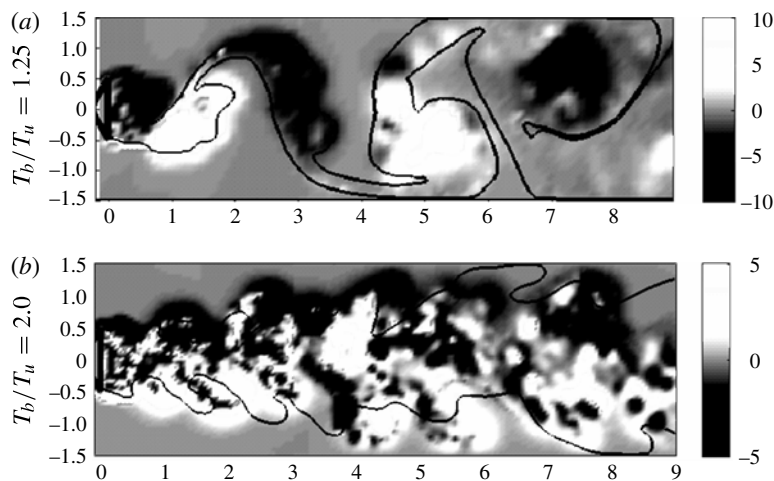
FIGURE 2. Computationally predicted vorticity field and instantaneous flame edge for two flame temperature ratios: (*a*) $T_b/T_u = 1.25$, (*b*) $T_b/T_u = 2$. Reproduced with kind permission from Erickson & Soteriou (2011).

well as large-amplitude sinuous motions of the flow field which resemble the von Kármán vortex street. Hertzberg *et al.* (1991) and Anderson *et al.* (1996) appear to have first used convective and absolute instability notions to explain various structural features in the flame/flow field, such as vortex shedding and near-blowoff flame dynamics.

The first systematic demonstration showing the effects of flame density ratio in combusting flows was presented by Erickson & Soteriou (2011) and is reproduced in figure 2. Their results show that a large sinuous flow feature gradually grows in prominence as density ratio across the flame is decreased below values of approximately 2–3. This observation is quite significant as it shows that the dominant fluid mechanics in a lab-scale burner with non-preheated reactants, which has a 'high' density ratio, can be very different from those of a facility with highly preheated reactants, such as many combustion applications. For example, stoichiometric methane air flames with reactant temperatures of 300 and 1000 K have density ratios of 7.5 and 2.6, respectively.

There have been no parallel experimental studies that have systematically studied flame density ratio effects on unsteady flow/flame features. The reason for this is that obtaining a stable (i.e. one that is not near blowoff) flame over a range of density ratios, particularly low density ratios, is quite difficult. Flames propagating into room-temperature reactants will blow off at density ratios much higher than where the phenomenon of interest occurs. For example, a methane/air flame at an equivalence ratio of $\varphi = 0.6$ and $T = 300$ K has a density ratio of $\rho_u/\rho_b = 5.6$. Increasing the equivalence ratio to $\varphi = 1.0$ leads to a density ratio of 7.5. This density ratio variation of ~25 % is all that is possible over the typical range of experimentally accessible fuel/air ratios for which a stable flame can be achieved when fuelled with reactants at standard temperature and pressure. In contrast, in a gas turbine combustor with a combustor inlet temperature of 800 K (Lovett *et al.* 2004) and equivalence ratio of 0.6, the flame temperature ratio is 2.6 for a methane–air flame. Similarly, high-efficiency

recuperated cycles or reheat cycles may have inlet temperatures of 1000–1100 K (Lovett *et al.* 2004; Aquaro & Pieve 2007), leading to temperature ratios of ∼2.

The implications of this absolute/convective instability distinction are particularly significant in thermoacoustic instability problems, where vortical structures excited by acoustic waves play important roles in the feedback mechanism (Lieuwen & Yang 2005). The 'convectively unstable' system is quite sensitive to acoustic excitation (Huerre & Monkewitz 1990). In contrast, the absolutely unstable system is an oscillator – it exhibits intrinsic, self-excited oscillations and does not require external disturbances to persist. In such a self-excited system, the limit-cycle behaviour may remain independent of the external forcing, unless the amplitude is high enough that the phenomenon of 'lock-in' occurs (Blevins 1977; Masselin & Ho 1985). In one case, low-amplitude acoustic excitation will induce a proportional response while in the other it may not. In turn, this has important implications for which type of flow instabilities can be involved in linear combustion instability mechanisms. For example, it suggests that simulating combustion instabilities in simplified lab combustors with high density ratios will lead to completely different acoustic–hydrodynamic stability coupling processes from what may be actually occurring in the low-flame-density-ratio application of interest.

The objectives of this study are two-fold. First, we experimentally characterize the unsteady flow evolution as the flame density ratio is monotonically varied across this bifurcation in flow structure. To do this, it is necessary to highly preheat the reactants to obtain flames that are stable (i.e. well removed from blowoff), yet of low density ratio. This was done by developing a facility capable of vitiating the flow, with independent control of the fuel/air ratio of the two burners. Such a facility is able to achieve broad ranges of flame density ratio. In order for these density ratio sweeps to be conducted at a fixed bluff-body lip velocity requires a second, independently controlled air injection source. The ability to control two independent air flows and two independent fuel/air ratios leads to substantial flexibility in operating conditions. Furthermore, great care was taken to stay well away from blowoff boundaries, where additional flame dynamics can occur (Shanbhogue *et al.* 2009a; Chaudhuri *et al.* 2010).

The second study objective is to compare the empirical results to the results of parallel stability theory and determine whether the transition in flow structure can be parameterized in the way suggested by theory; in particular, to determine if the density and backflow ratios have the same measured effect as theory would suggest they do. We will show that they that do, but that the relative offset between the temperature and velocity gradients also has a very significant influence on the results.

2. Experimental facility, diagnostics, and testing procedures

The experimental rig, shown in figures 3 and 4, consists of two premixed, methane–air combustors in series. The first combustor is used to vitiate the flow. The second, bluff-body-stabilized, combustor consists of a rectangular section with a bluff body spanning the width of the combustor, creating a nominally two-dimensional flow. The aspect ratio of bluff-body height to chamber width is 0.15. This combustor has quartz windows for optical access from all four sides. Two different bluff bodies were used in the test section: a two-dimensional ballistic shape (shown in figure 5a), and a v-gutter (shown in figure 5b). From here on, the two-dimensional ballistic shape will be referred to as the ballistic bluff body.
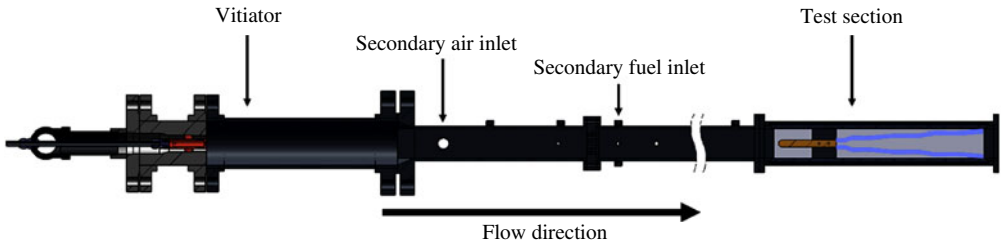
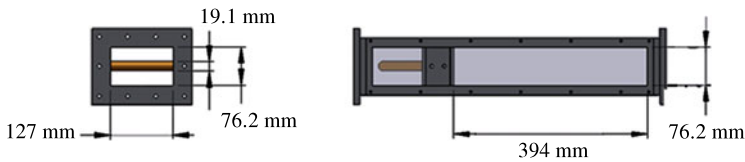FIGURE 3. (Colour online) Schematic of the atmospheric pressure, vitiated, bluff-body rig.

FIGURE 4. (Colour online) Schematic of test section with ballistic bluff body installed.
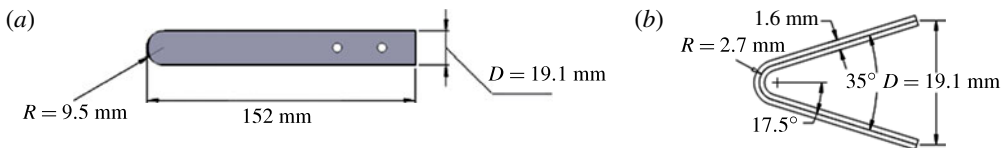

FIGURE 5. Schematics of bluff bodies: (*a*) ballistic; (*b*) v-gutter.

Primary air and fuel were premixed upstream of the vitiator. Secondary air and fuel were plumbed into the rig and premixed in a 1.4 m long settling section aft of the vitiator, and upstream of the test section. Fuel is inserted from a manifold of eight injectors, each of which penetrates 2.5 cm into the flow; three injectors pass through the top wall, three through the bottom wall, and one injector passes through each sidewall. The natural gas concentration entering the test section was analysed as a function of position on the plane at this axial position, and was uniform within $\pm 10\%$; uniform equivalence ratio was assumed and the effects of non-uniform equivalence ratio (Anselmo-Filho *et al.* 2009; Chaudhuri & Cetegen 2009; Kim & Hochgreb 2011) were not considered. The primary and secondary air and fuel each have their flow rates adjusted individually. This design allows the flame density ratio and bluff-body lip velocity to be varied independently in the test section, by adjusting the air flow rates and stoichiometries in the vitiator and test section separately. The test matrix was developed such that primary and secondary air flow rates and primary and secondary equivalence ratios could be adjusted to achieve a variety of density ratios at a fixed velocity.

Mass flow rates for the primary and secondary air and fuel were measured across calibrated knife-edge orifice plates using the static upstream pressure and the differential pressure across the plate, measured with Omega PX209 solid-state pressure transducers and Omega PX771A differential pressure transmitters, respectively. The temperature just upstream of the test section (after addition of secondary air and fuel)

was measured by a type K thermocouple and an Omega TX13 transmitter. Values were recorded once every second for ten seconds, and then averaged.

It will be helpful now to define several reference velocities which will be used throughout this paper. Bluff-body lip velocities quoted in this paper are calculated using the formula $U_{lip} = \dot{m}_{lip}/(\rho_{lip}A_{lip})$ (where $\dot{m}_{lip}$ is the mass flow rate), which is an average axial flow velocity. The density for the lip velocity calculation (ρ_{lip}) was determined from the temperature measured just before the test section and the gas composition of the secondary air and fuel adiabatically mixed with the equilibrium vitiated gas. An equilibrium gas solver was then used to calculate the adiabatic density ratio across the test-section flame. The area, A_{lip}, is the cross-sectional area of the flow at the plane of the bluff-body trailing edge. Another velocity, which will be used as a reference in the stability analysis in later sections, is the average velocity. This is defined as the average velocity between the inner stream and an outer stream (see figure 1*a*), $U_{av} = (U_u + U_b)/2$, and is a function of axial position. Finally, a velocity difference will be defined as $\Delta U = U_u - U_b$.

For the 50 m s^{-1} cases, the uncertainty in measured gas flow rates and the resulting temperature and density ratios was ~2 %. For the 20 m s^{-1} cases, uncertainty was ~4 % for the measured gas flow rates, and ~10 % for the temperature and density ratios. Uncertainties are bounded by worst-case combinations of maximum and minimum flow rates and thermocouple readings for a given test. Uncertainty in thermocouple readings was less than 1 %.

Test matrix design was motivated by figure 1(*b*). Actual conditions tested are overlaid on the stability map in the figure, where the backflow ratio β_{max} was determined from the maximum value of β (which itself varies axially). Note that the ballistic bluff body provides a lower maximum backflow ratio than the v-gutter. Contours of constant $\omega_{0,i}D/(2U_{av})$, corresponding to the absolute spatio-temporal growth rate as computed from temperature and velocity measurements in conjunction with linear stability theory, are provided as well. These theoretical values are calculated assuming top-hat density and velocity profiles, parallel flow, and high Reynolds number. While the simplified, parallel stability analysis was useful for parameterizing the stability problem and designing the test matrix, a numerical local stability analysis was performed to compare stability theory results to experimental observations. This analysis is discussed later in the section on comparisons with local stability analysis.

Experimental diagnostics consisted of high-speed, line-of-sight imaging of flame chemiluminescence, high-speed particle image velocimetry (PIV), and laser Doppler velocimetry (LDV). High-speed chemiluminescence imaging was performed with a Photron Fastcam SA3 camera at a 3000 Hz frame rate and 512×256 pixel resolution. This CMOS camera operates nearly continuously at 3000 Hz. The flame was imaged through a BG-28 filter for chemiluminescence imaging. This filter transmission exceeds 10 % for wavelengths between 340 and 630 nm, and peaks at 82 % transmission at 450 nm. The flame was imaged from the bluff-body trailing edge to approximately nine bluff-body diameters downstream. A total of 8029 images were stored in each run.

High-speed PIV measurements were obtained with a LaVision Flowmaster Planar Time Resolved system. The laser is a Litron LDY303He Nd:YLF laser with a wavelength of 527 nm and a 5 mJ pulse^{-1} pulse energy at a 10 kHz repetition rate. The Photron HighSpeed Star 6 camera was operated with a pixel resolution of 640×448 at a frame rate of 10 kHz. A BG-28 optical filter was placed in front of the camera for removal of red and infrared radiation during reacting tests. The flow

was seeded with 5 μm Al_2O_3 particles. This ceramic material was chosen due to its durability in reacting flows and its high refractive index (Melling 1997). This particle size was chosen because it is large enough to resist accumulation on and clouding of the test-section windows. Simultaneously, this particle size has a sufficiently small Stokes number to accurately track the flow. Following the work by Mei (1996), the Stokes number calculated for this flow and seed particle combination was 0.006. This Stokes number is based on 5 μm seeding particles, with environmental kinematic viscosity of 3×10^{-4} m^2 s^{-1}, and oscillation frequency of 600 Hz (roughly the highest global mode frequency encountered). The high temperature and corresponding high viscosity in the test section facilitate the use of such a particle. This Stokes number is comfortably below the cutoff Stokes number for solid particles in air (Mei 1996), which is in the range of 0.02–0.04 and would correspond to a frequency of 13.8 kHz.

The DaVis 7.2 software from LaVision was used to process the PIV data, performing background subtraction and then calculating the velocity fields. All velocity calculations were performed using the LaVision multi-pass method; this consisted of a single pass with 64×64 pixel interrogation windows and 50 % overlap between interrogation windows, followed by two passes with 32×32 pixel interrogation windows and 50 % overlap between the interrogation windows. Post-processing on the velocity vectors was also performed as follows. For 50 m s^{-1} cases, any velocity vector with an axial component outside of the ± 90 m s^{-1} range or a transverse component outside of the ± 45 m s^{-1} range was discarded. For 20 m s^{-1} cases, the accepted range of axial velocities was ± 36 m s^{-1} and for transverse velocities was ± 18 m s^{-1}. Furthermore, velocity vectors whose velocimetry calculation had a peak correlation coefficient less than 0.2 were discarded, as were neighbouring vectors whose ratio of difference to average velocity magnitude was greater than 20 % of the r.m.s. of the nearest neighbours.

Studies were performed with two fields of view and corresponding resolutions. The larger field of view was nominally 250 mm long in the axial direction and 80 mm wide in the transverse direction, leading to a velocity field resolution of 4.8 mm using a 50 mm lens. The smaller field of view was 100 mm $\times$ 80 mm with a velocity field resolution of 3.0 mm using an 85 mm lens. A total of 2000 PIV image pairs was taken at a frame rate of 10 kHz with 12 μs between images for a given pair.

The flame density ratio was estimated from an equilibrium solution for the adiabatic flame temperature, using the measured approach-flow temperature and using a gas composition determined from an adiabatic mixing calculation of the secondary air, fuel, and equilibrium vitiated gas. In addition, the time-averaged density field distribution was determined from Mie scattering images (taken from the raw PIV images). From these images, an instantaneous flame sheet position can be readily extracted because of the sharp jump in seed particle density. The instantaneous density was then specified as a binary field having either the burned or unburned value. These instantaneous values were then averaged at each location to obtain the temporally averaged density field. The key assumption behind this procedure is that the flame is very thin relative to bluff-body diameter, which is well satisfied for this problem, as verified by detailed chemical kinetic calculations of an unstretched, premixed flame (using GRI 3.0) showing that the estimated flame thickness is roughly 2 % of the bluff-body diameter.

Two-component LDV was used to measure the boundary layer thickness at the trailing edge of the bluff body. Seeding material consisted of 5 μm aluminium oxide, whose frequency response characteristics were discussed previously. For each measurement volume, data acquisition was limited to either 30 s or 5000 counts,
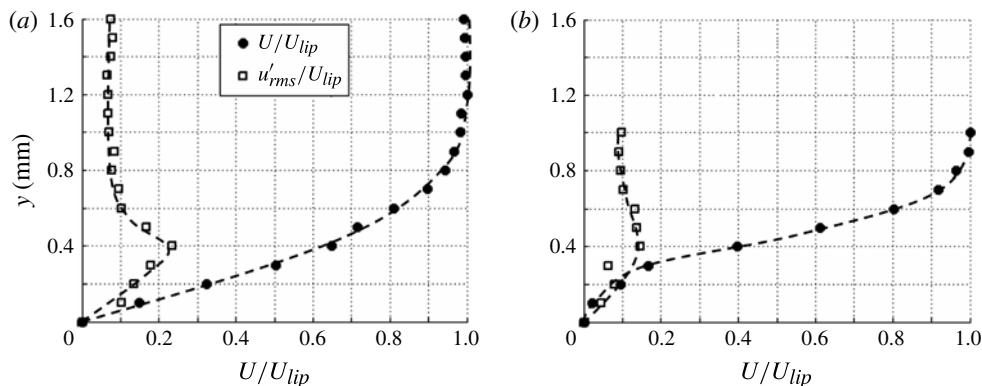
FIGURE 6. Boundary layer profiles for the v-gutter at $U_{lip} = 50$ m s^{-1}, and a density ratio of (a) $\rho_u/\rho_b = 1.7$ and (b) $\rho_u/\rho_b = 2.5$, showing point of inflection.

whichever came first. The acquisition channel used for axial velocity measurements used a laser wavelength of 514.5 nm, a fringe spacing of 7.9196 µm, a beam waist of 70.19 µm, and a Bragg cell frequency of 40 MHz. The resulting low and high velocity limits were -24 m s^{-1} and 119 m s^{-1}, respectively. The acquisition channel used to measure the transverse velocity used a laser wavelength of 488 nm, a fringe spacing of 7.5117 µm, a beam waist of 66.57 µm, and a Bragg cell frequency of 40 MHz. For this channel, the low and high velocity limits were -68 and 68 m s^{-1}. Both channels had a focal length of 300 mm, a beam separation of 19.5 mm, a beam diameter of 2.8 mm, and used a 20 MHz high-pass filter.

3. Results: time-averaged flow features

This section summarizes the time-averaged flow characteristics and inflow conditions. These data are useful as inputs for flow stability or computational predictions. We first present high-resolution, LDV-based measurements of the inflow conditions. Then, we present PIV-based measurements of the time-averaged and fluctuating root-mean-square (r.m.s.) velocity field characteristics. Several important flow parameters are then extracted from these data, including recirculation zone length, location and value of peak reverse flow velocity in the wake, and the dependence of these quantities upon density ratio. All of these parameters have important implications for flow stability characteristics.

Consider first the inflow conditions. Two-dimensional LDV measurements were obtained at the bluff-body trailing edge by scanning the flow transversely in steps of 0.1 mm, as shown in figure 6. The velocity components measured were the axial velocity, u, and the transverse velocity, v. These data show that the separating boundary layer approaches the free-stream velocity at a distance of ~ 1 mm from the flameholder. The momentum thickness was calculated with the relation:

$$\theta = \int_{y/D=0}^{y/D=2} \left[\frac{1}{4} - \left(\frac{U - U_{av}}{|\Delta U|} \right)^2 \right] \, \mathrm{d}y \qquad (3.1)$$

yielding $\theta = 0.14$ and $\theta = 0.09$ mm for $\rho_u/\rho_b = 1.7$ and $\rho_u/\rho_b = 2.5$, respectively, for the v-gutter at $U_{lip} = 50$ m s^{-1}. This leads to a most-amplified frequency for the Kelvin–Helmholtz instability in the shear layers of $f_{KH} = 11$ kHz and $f_{KH} = 18$ kHz

Bluff body	U_{lip} (m s^{-1})	ρ_u/ρ_b	u'_{rms}/U_{lip}	θ (mm)	f_{KH} (Hz)
V-gutter	50	1.7	0.08	0.14	11 000
V-gutter	50	2.5	0.10	0.09	18 000
V-gutter	20	1.9	0.15	0.15	4 300
V-gutter	20	3.2	0.15	0.20	3 200
Ballistic	50	1.7	0.16	0.25	6 400
Ballistic	50	2.5	0.13	0.17	9 400
Ballistic	20	1.9	0.22	0.26	2 500
Ballistic	20	3.2	0.23	0.16	4 000

TABLE 1. Measured momentum thickness and estimated Kelvin–Helmholtz frequency, as well as outer flow turbulence intensity, for several bluff bodies and flow conditions.

respectively using the relation (Ho & Huerre 1984)

$$f_{KH} = 0.032 \frac{U_{lip}}{\theta}. \tag{3.2}$$

The lower temperature ratio case has a thicker boundary layer since the reactant temperature (and therefore viscosity) for low temperature ratio cases is higher than that for high temperature ratio cases. In comparison to the v-gutter, the momentum thickness at the ballistic-bluff-body trailing edge was somewhat higher, as would be expected because of the boundary layer's longer development length in this case. For most cases, the momentum thickness at the trailing edge of the ballistic bluff body was 1.7 times that of the v-gutter. Measured momentum thickness values and estimated f_{KH} values are presented in table 1 for both bluff bodies at the conditions tested with LDV.

Returning to figure 6, note the differences in the near-wall velocity profile in the high and low temperature ratio cases. This is due to heat transfer from the hot bluff body to the boundary layer. In the high temperature ratio case, the v-gutter becomes very hot with respect to the much cooler reactant temperature; therefore there is heat conduction from the flame holder to the reactant gas. This is a destabilizing effect (Schlichting & Gersten 2000), and leads to a point-of-inflection profile (as evidenced by the data in figure 6b). However, no boundary layer separation was observed, as shown by the data in the figure. The profiles for the high temperature ratio case are 'clipped' at 1 mm because of thermal expansion of the v-gutter in the transverse direction (again, because the flameholder becomes very hot for this case), which obscured the first 1/2 mm of the transverse scan. The rig is restrained such that axial thermal expansion is not a concern.

The measured r.m.s. axial velocity u'_{rms} is plotted as a function of transverse position in figure 7. Inflow turbulence intensity, $u'_{rms}(y)/U_{lip}$, was ~9 % in the outer flow and ranged from roughly 15 % to 25 % in the boundary layers for the v-gutter at $U_{lip} = 50$ m s^{-1}.

Consider next the time-averaged flow features downstream of the bluff body. Figure 8 plots the dependence of the time-averaged axial flow field along both axial and transverse cuts. These results were produced from the higher resolution PIV measurements. Start with figure 8(a), which plots the axial variation of the velocity at two transverse locations, corresponding to the bluff-body centreline and one half-diameter beyond the bluff-body lip. The figure illustrates how the reverse flow in the recirculation zone evolves with axial position, reaching a maximum reverse flow velocity at a location denoted as L_{max} which is typically ~1.5 bluff-body diameters
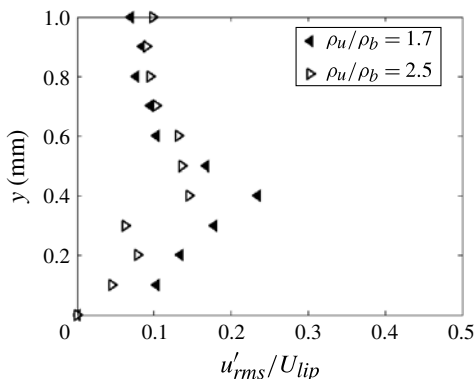
FIGURE 7. LDV measurement of the turbulence intensity at the bluff-body trailing edge, as a function of transverse position, for the v-gutter at $U_{lip} = 50$ m s^{-1}.
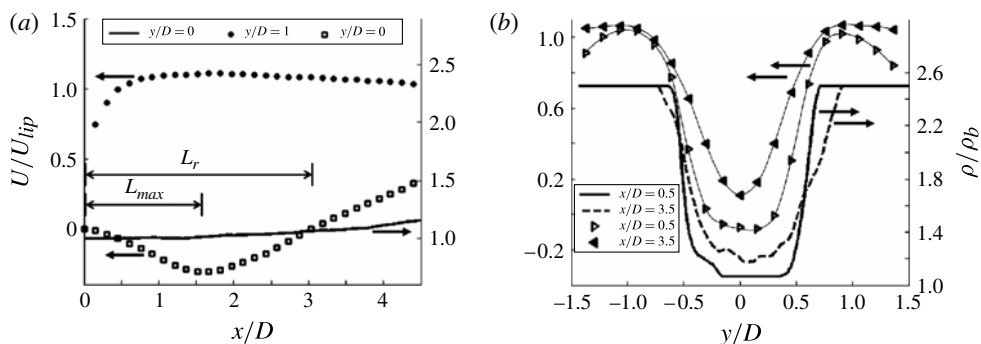

FIGURE 8. Mean axial velocity (symbols) and density profiles (lines), showing (*a*) axial profiles and (*b*) transverse profiles for the ballistic bluff body at $U_{lip} = 50$ m s^{-1}, $\rho_u/\rho_b = 2.5$. Arrows indicate which axis of ordinates belongs to which dataset.

downstream. The recirculation zone length, L_r, is also indicated on the figure. The transverse profiles of axial velocity are shown in figure 8(*b*). These transverse profiles of axial velocity, taken at fixed axial positions, illustrate the recirculation zone and wake profile characteristics. The corresponding mean density profiles are overlaid. Note that the thickness of the density gradient is slightly less than, although comparable to, that of the shear layer at a given axial position. Note also that the point of inflection of the average density profile is located near that for the velocity. In general, near the bluff body the flame tends to sit closer to the flow centreline than the shear layer point of inflection ('inboard' of the shear layer), whereas farther downstream the flame tends to sit farther from the flow centreline ('outboard' of the shear layer).

The effect of density ratio on the recirculation zone characteristics is illustrated in figures 9 and 10. These plots show that the recirculation zone length generally increases with density ratio. This seems to be consistent with the idea that recirculation zone length increases as large-scale vortex shedding is suppressed (Pan, Vangsness & Ballal 1992; Cardell 1993; Shanbhogue 2008). Furthermore, the magnitude and location of peak reverse velocity also increase with density ratio.
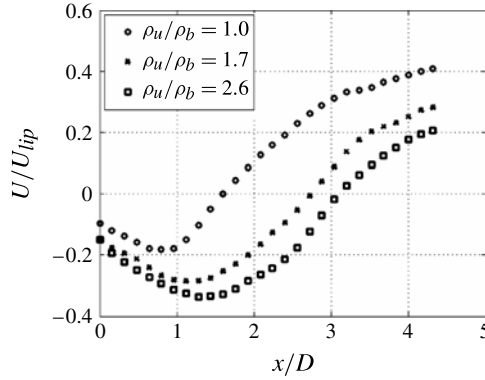
FIGURE 9. Centerline time-averaged velocity for the v-gutter at various density ratios and $U_{lip} = 50 \text{ m s}^{-1}$.
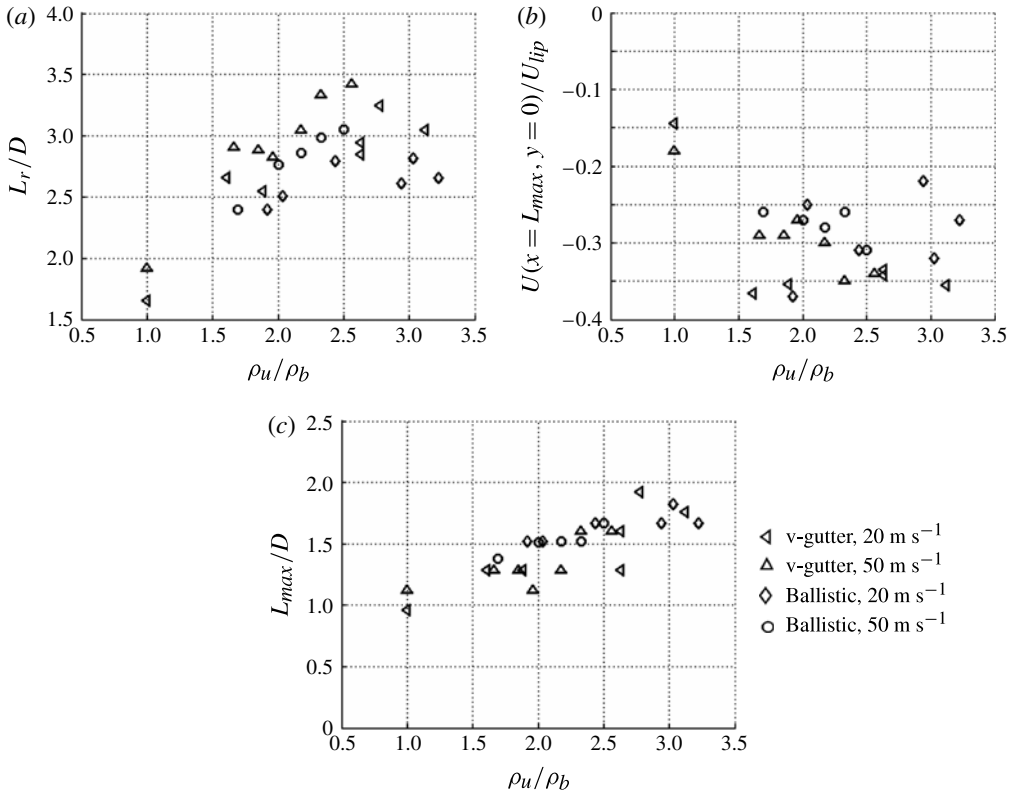

FIGURE 10. Dependence of the recirculation zone geometry on the density ratio, showing (*a*) the recirculation zone length, (*b*) the peak backflow velocity and (*c*) the axial location of peak backflow velocity.
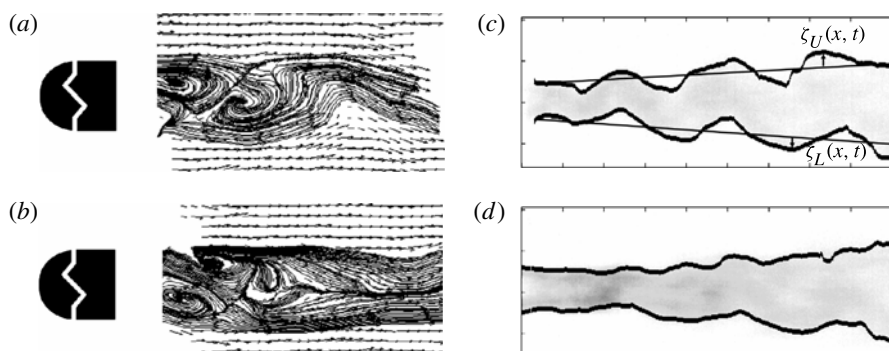
FIGURE 11. Typical instantaneous visualizations of flame and flow structure for the ballistic bluff body with $U_{lip} = 50$ m s^{-1} at two density ratios, showing (*a*) streamlines at $\rho_u/\rho_b = 1.7$, (*b*) streamlines at $\rho_u/\rho_b = 2.4$; (*c*) flame with edge tracking at $\rho_u/\rho_b = 1.7$ and (*d*) flame with edge tracking at $\rho_u/\rho_b = 2.4$.

Both of these latter parameters have important implications for convective/absolute instability of the flow, as well as locations of pockets of absolute instability. It is important to remember, however, that these data are obtained under 'limit-cycle' conditions and that the reverse flow velocities are presumably affected by the global instability of the flow under the lower density ratio conditions. Finally, the data show a much weaker dependence of recirculation zone characteristics on velocity, consistent with previous observations (Potter & Wong 1958).

4. Results and analysis: flame and flow dynamics

4.1. *Spectral and correlation analysis*

This section describes key dynamical characteristics of the flame and flow dynamics. Results are primarily presented for the ballistic bluff body at a lip velocity of 50 m s^{-1}, which are quite representative of results observed at other conditions. Discussion is included where qualitatively different results are observed at other conditions. In order to present a qualitative picture of the flow first, figure 11 illustrates typical instantaneous streamlines and flame images from low and high density ratio flames. The flame images show clear, spatially sinuous undulations at low density ratios which largely disappear at higher density ratios. These observations are in agreement with previous experiments (Kiel *et al.* 2007) and computations (Erickson & Soteriou 2011) reviewed in § 1.

Flame dynamics were quantified using the transverse positions of the top and bottom flame branch edges, $\zeta_U(x, t)$ and $\zeta_L(x, t)$, as functions of axial position and time, as shown in figure 11(*c*). This resulted in time series for edge positions along both flame branches at each axial position. These time series are Fourier transformed to determine their temporal spectra, given by $\hat{\zeta}_U(x, f)$ and $\hat{\zeta}_L(x, f)$.

PIV data were used for corresponding analysis of flow-field dynamics. PIV data shown in this section were taken from the transverse velocity along the combustor centreline, $v(x, y = 0, t)$ whose Fourier transform is given by $\hat{v}(x, y = 0, f)$. The rest of this section summarizes the key results obtained from analysis of the time series and spectra of both flame and flow dynamics as functions of flame density ratio.
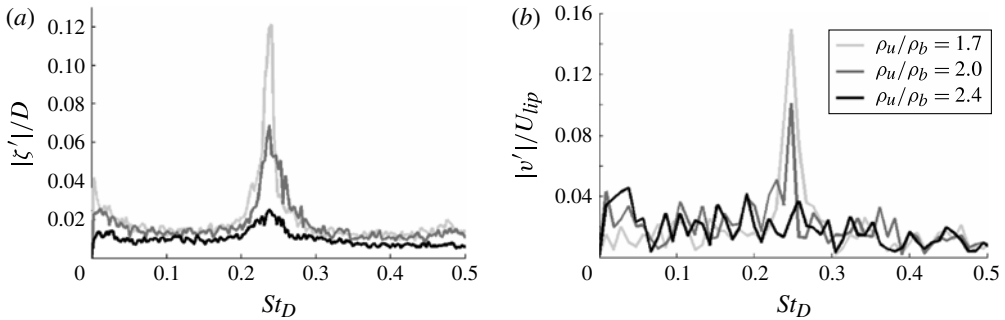
FIGURE 12. Spectra for the ballistic bluff body at $U_{lip} = 50\ \mathrm{m\ s^{-1}}$ at the axial position of peak response for (*a*) upper flame edge position and (*b*) centreline transverse unsteady velocity magnitude.

Figure 12 presents the flame and flow spectra at their axial positions of peak magnitude, for three density ratios, as functions of Strouhal number, $St_D = fD/U_{lip}$. Figure 12(*a*) shows this result for the upper flame edge. At the highest density ratio shown, $\rho_u/\rho_b = 2.4$, spectral energy is broadly distributed across all frequencies, with a small bump at $St_D \sim 0.24$. As the density ratio is decreased to 2.0, a clear feature appears centred near $St_D = 0.24$. As the density ratio is further decreased to 1.7, the response at $St_D = 0.24$ becomes narrowband and quite prominent. Figure 12(*b*) shows spectra of the unsteady transverse velocity for the same flow conditions, and demonstrates that the flow similarly exhibits a growing narrowband spectral feature at $St_D = 0.24$.

Figure 13 overlays the axial development of the above spectra at $St_D = 0.24$. These plots emphasize the growth, peak and decay of the flame and the flow responses. These non-monotonic flame spectra envelope results are typical of those measured in flames forced by narrowband disturbances and reflect the additional effect of flame anchoring and kinematic restoration (Shanbhogue *et al.* 2009*b*). Notice that the flame response and the flow response are related, as would be expected. The peak flame response occurs a few bluff-body diameters downstream of the peak flow response, and a stronger flow response results in a stronger flame response.

In order to focus on the characteristics near the frequency of peak response, the integrated power under the spectral peak between Strouhal numbers of 0.20 and 0.28 is computed as a function of density ratio. This energy is converted to an r.m.s. of the signal at the response frequency by use of Parseval's theorem, using the relation below that relates the r.m.s. of the time series $s(t)$ of duration T and spectrum $\hat{s}(f)$,

$$s_{rms} = \sqrt{\frac{1}{T} \int_{f^-}^{f^+} \left| \hat{s}(f) \right|^2 \mathrm{d}f}. \tag{4.1}$$

These r.m.s. values are presented in figure 14 for both the flame and the fluctuating velocity. The flame data in figure 14 show that the normalized fluctuation in flame position has a value of roughly 4 % over the $2.4 < \rho_u/\rho_b < 3.4$ range. Below a value of $\rho_u/\rho_b = 2.4$, the response gradually increases to 18 % at $\rho_u/\rho_b = 1.7$. Similar behaviour is shown by the velocity data. This plot also indicates that the transition in flow and flame characteristics is not an abrupt bifurcation with change in density ratio, but a more gradual increase in narrowband response as the density ratio decreases.
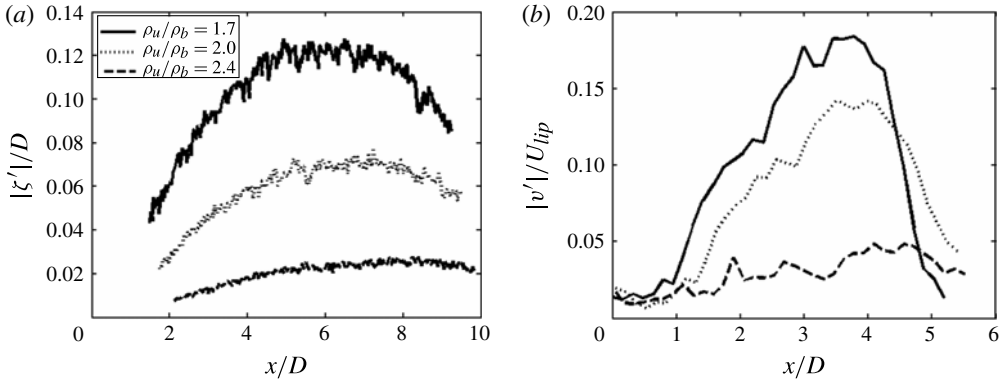
FIGURE 13. Axial profiles of (*a*) the flame and (*b*) the flow, showing the response at $St_D = 0.24$ for the ballistic bluff body at $U_{lip} = 50$ m s^{-1}.
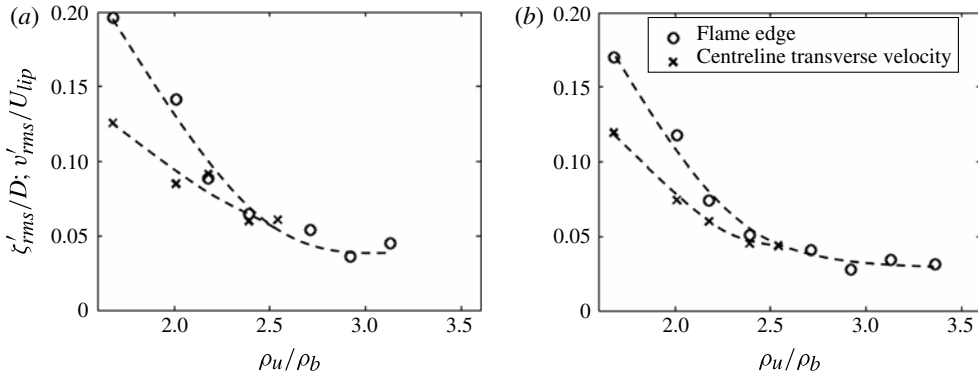

FIGURE 14. Dependence of narrowband spectral energy ($0.2 < St_D < 0.28$) upon density ratio for ballistic bluff body at $U_{lip} = 50$ m s^{-1}, expressed as r.m.s. flame edge fluctuation averaged over both flame branches, and r.m.s. centreline transverse velocity. Measurement was taken at (*a*) the axial position of peak response and (*b*) $x/D = 3.5$.

The correlation coefficient between the two flame branches, $r_{U,L}$, defined

$$r_{U,L}(x) = \frac{\langle \zeta_U(x, t) \zeta_L(x, t) \rangle}{\sqrt{\langle (\zeta_U(x, t))^2 \rangle \langle (\zeta_L(x, t))^2 \rangle}}, \quad (4.2)$$

provides important information on the scale and/or correlation between the underlying flow structures perturbing them.

Note that negative and positive correlation coefficients imply asymmetric and symmetric flame wrinkling, respectively. Furthermore, a nearly zero correlation coefficient implies that the flame branches are disturbed by uncorrelated structures with a scale much smaller than their transverse separation distance. The dependence of the correlation coefficient upon ρ_u/ρ_b is plotted in figure 15, showing that the correlation coefficients are near zero, but slightly positive, for $\rho_u/\rho_b > \sim 2.5$. The correlation coefficient monotonically decreases towards values of $r_{U,L} \sim -0.6$,
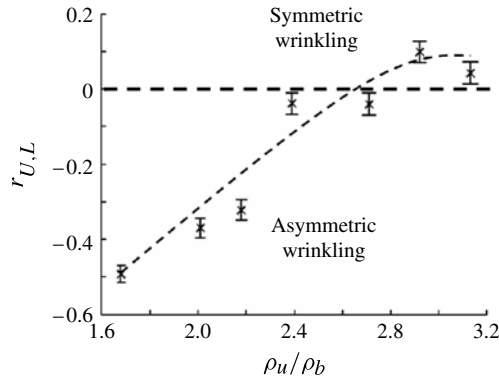
FIGURE 15. Correlation coefficient between top and bottom flame edge position for the ballistic bluff body at $U_{lip} = 50 \text{ m s}^{-1}$. Measurement was taken at the axial position of peak flame response.

indicative of growing correlation and asymmetric motion with decreasing flame density ratio.

To summarize these data, figure 14 shows that there is a gradual increase in spectral energy at the asymmetric vortex shedding frequency as density ratio is decreased. Figure 15 shows a gradual increase in asymmetry and coherence between the two flame branches for decreasing ρ_u/ρ_b, suggesting the appearance of large structures in the wake. The very narrowband spectral nature of the flow in figure 12 suggests that the flow evolves to a limit-cycling, globally unstable flow at low density ratios. Simultaneously, the limit-cycle amplitude of the global mode grows monotonically in amplitude with decreases in density ratio for $\rho_u/\rho_b < 2.4$. The next section compares these results to those derived from parallel stability analyses.

4.2. *Comparisons with local stability analysis*

This section compares and correlates several of the above described data characteristics to predictions from a locally parallel stability analysis with top-hat velocity and density profiles as sketched out in § 1. In order to plot the experimental tests on the stability map shown in figure 1(b), knowledge of the backflow ratio and density ratio was required for each condition. The centreline and free-stream axial velocity fields obtained from PIV data were used to calculate the velocities needed to quantify the backflow ratio, $\beta(x)$. The measured local backflow ratio (corresponding to a flow profile at a given axial position) and density ratio were then inserted into the high-Reynolds-number dispersion relation from Yu & Monkewitz (1990) in order to map temporal growth rates onto the complex k-plane. Saddle points were located and verified to be valid k^+/k^- pinch points. The growth rate at such a saddle point corresponded to a local, predicted absolute spatio-temporal growth rate, $\omega_{0,i}$; this process was then repeated at each axial position, for each test condition.

In addition to this simplified analysis, a numerical analysis was performed which took the measured mean velocity and density profiles as inputs. The absolute growth rate, ω_0, and absolute wavenumber, k_0, were calculated at each axial station by performing a spatio-temporal stability analysis on the time-averaged velocity and density profiles. The linearized, low-Mach-number Navier–Stokes equations were reduced to four ordinary differential equations in four primitive variables (u, v, w, p), which were solved using Chebyshev spectral methods on Gauss–Lobatto spaced

gridpoints. The procedure is described in previous work performed at Cambridge University (Rees 2009; Rees & Juniper 2010; Juniper, Tammisola & Lundell 2011). Saddle points were found in the complex k-plane and verified to be valid k^+/k^- pinch points (Huerre & Monkewitz 1990). The valid saddle point with the highest absolute growth rate was labelled the dominant saddle point. If the absolute growth rate of this saddle point is greater than zero then this slice of the flow is absolutely unstable. These data are somewhat noisier than those that would be obtained from assuming a top-hat velocity profile but are preferred because they use the actual velocity and density profiles. This noisiness stems from the strong sensitivity of the growth rate to the small, but highly significant, transverse shifts in relative locations of gradients in the density and velocity profiles.

Isocontours of the non-dimensional absolute growth rate, $\omega_{0,i}D/(2U_{av})$, are presented in figure 16. This figure plots calculated absolute growth rate contours as functions of axial position and density ratio for both bluff bodies at lip velocities of 50 and 20 m s^{-1}. Each of these plots was compiled from the measured velocity fields for a given bluff body, lip velocity, and tests at several density ratios. The plots show that regions of largest local absolute instability, $\omega_{0,i}D/(2U_{av}) > 0$, occur at low density ratios and at axial positions of roughly $x/D \sim 3/2$ near where the reverse flow velocity is highest. The spatial extent of these predicted absolute instability pockets grows with decreasing density ratio. Note that the absolute instability region does not start immediately aft of the bluff body, because of the low backflow velocities immediately downstream of the bluff body.

Note that the predictions obtained from the model profile shown in figure 1(*a*) and the calculations obtained from the actual measured profiles are qualitatively similar. However, a key quantitative difference between the two is the larger growth rates, and the prediction of absolute instability for a much broader range of density ratios, obtained from the computed results that used the measured profiles. For example, consider figure 16(*c*,*d*), showing local absolute stability results for the ballistic bluff body at 20 m s^{-1}. At a density ratio of $\rho_u/\rho_b = 2.6$, the analytical solution predicts the flow to be convectively unstable at all spatial positions using the simple profile, while the flow is predicted to have a pocket of absolute instability with the numerical computation.

This difference is due to two important simplifications of the model density and velocity profiles used for the simplified calculation: (i) collocated density and velocity jumps and (ii) an infinite domain. For Reynolds numbers larger than around 10^2, confinement destabilizes the sinuous mode in wake flows such as these, as discussed by Rees & Juniper (2010). Further effects which influence the stability prediction and are not accounted for by the simplified analysis, such as no-slip boundary conditions and global versus local results, are detailed by Juniper *et al.* (2011). In addition, the absolute-instability growth rate is a very sensitive function of the relative locations of the gradients in density and velocity. In order to illustrate this point, the model profile shown in figure 1(*a*) was generalized to include confinement and non-collocated density and velocity jumps. This analysis is summarized in the Appendix, which provides the generalized dispersion relation for the sinuous mode. Figure 17 plots the dependence of the density ratio of the absolute/convective instability transition upon the density–velocity jump offset, $\delta_\rho - \delta_u$. These results are shown at a fixed backflow of $\beta = 0.25$ and both with and without confinement. The velocity jump is located at a distance (from the centreline) corresponding to the bluff-body half-width, and the confinement was chosen to match the experimental facility. The plot shows the strong destabilizing effects of non-collocated density and shear layers, as well as confinement.
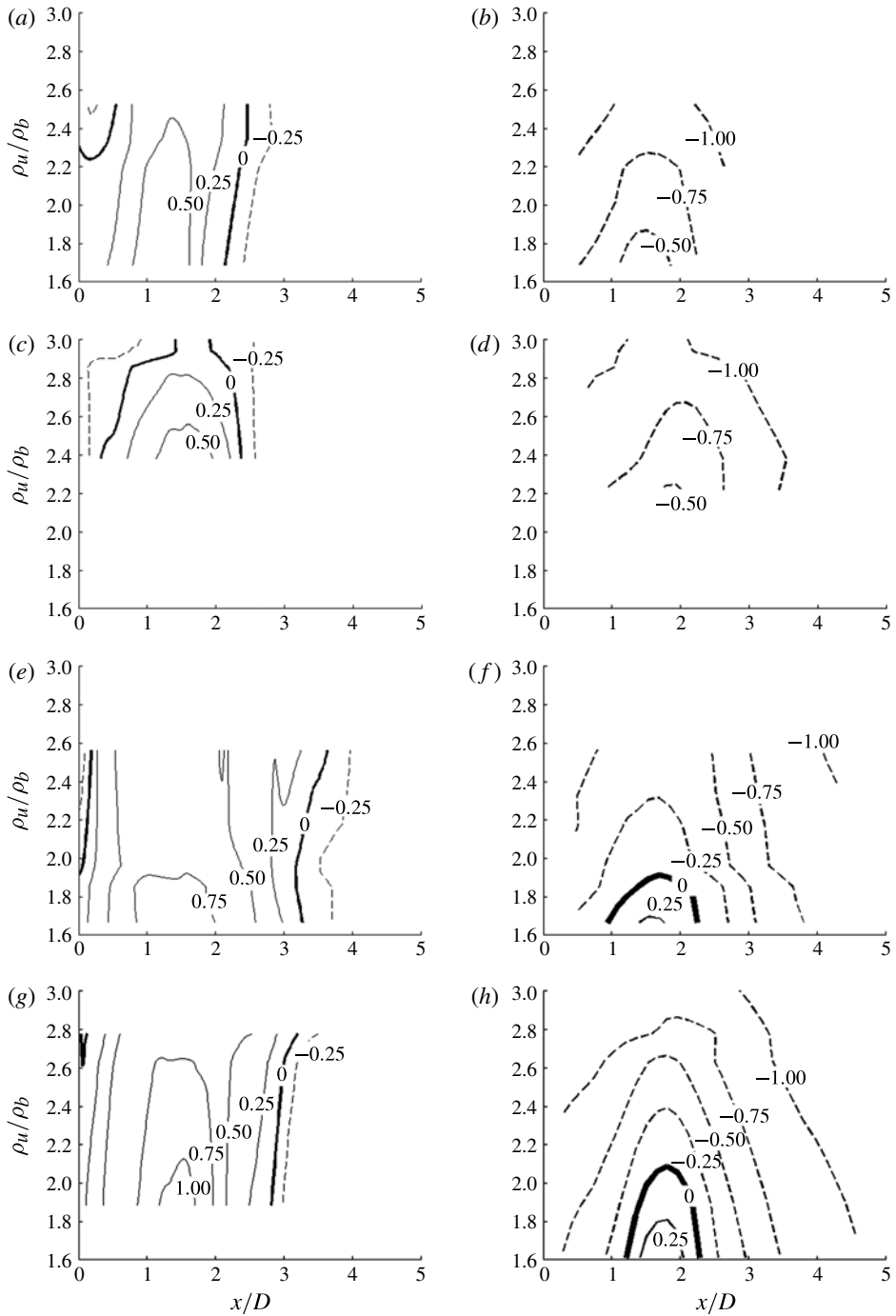
FIGURE 16. $\omega_{0,i}D/(2U_{av})$ contour maps versus axial position and density ratio, for: (a,b) ballistic bluff body at $50\,\mathrm{m\,s^{-1}}$; (c,d) ballistic bluff body at $20\,\mathrm{m\,s^{-1}}$; (e,f) v-gutter at $50\,\mathrm{m\,s^{-1}}$; (g,h) v-gutter at $20\,\mathrm{m\,s^{-1}}$. Column (a,c,e,g) shows numerical results from smoothed data, column (b,d,f,h) shows analytical results from top-hat profiles. Contour levels are labeled on the plots.
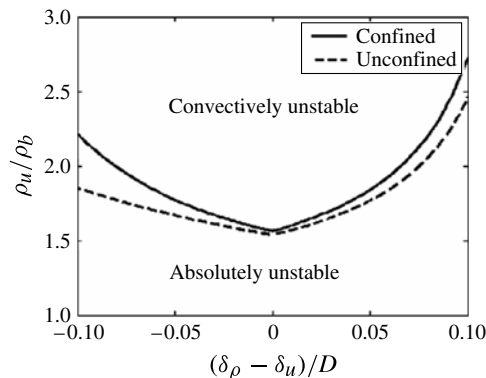
FIGURE 17. Stability limit as a function of the density–velocity jump offset, for a constant backflow ratio of $\beta = 0.25$, a velocity jump located at the bluff-body half-width ($\delta_u/D = 0.5$), and for the confined case a geometry of $H/D = 2$.

For example, begin with collocated velocity and density jumps for the unconfined case. If the velocity jump location is held fixed, and the density jump is shifted away from (outside of) the flow centreline by 10 % of its original position, then the density ratio for the absolute/convective (AI/CI) transition increases by 50 %, from about 1.6 to 2.4. Adding confinement on top of this further shifts the density ratio for the AI/CI transition to ∼2.7.

The basic trends in figure 17 (i.e. that a shift in the relative positions of velocity and density gradients away from one another, in either direction, is destabilizing), can be understood from the two limiting cases. If the density layers are moved far outboard of the shear layers, the wake and its shear layers essentially sit in a uniform-density fluid, and the stability boundary tends toward that of the iso-density case. The same result may be expected if the density layers are moved inboard to the flow centreline; in this case, the density ratio becomes an increasingly irrelevant quantity since the inner density region becomes pinched into a progressively smaller slab along the centreline, and again the wake effectively sits in a uniform-density fluid. Indeed, it can be shown that the dispersion relation in the Appendix limits to the uniform-density case in these two extremes.

Having shown that the basic trends in figure 17 can be understood from limiting cases, we next discuss the significant sensitivity of the stability boundary to even very small changes in relative locations of the gradients. This point is both predicted by the analysis and borne out by the comparisons between the measurements and the two different stability calculations. The strongly stabilizing effect of non-collocated density and shear layers on flow stability has been observed previously in direct numerical simulations (DNS) of a variable-density jet flow by Nichols, Schmid & Riley (2007), who showed that a small degree of misalignment materially changes the flow stability characteristics. It should be noted that because they studied low-density-ratio jets, this misalignment was a stabilizing effect, in contrast to the destabilizing effect it has in our low-density-ratio wakes.

For both two-dimensional jets and wakes, the global stability of the system is crucially affected by the nature of the interactions between the two shear layers. In particular, the two shear layers which would be nominally convectively unstable in isolation, interact with each other to cause global instability for the wake problem. The

spatial variations in density influence these interactions through two processes which are shown in the following vorticity equation, baroclinic torque and gas expansion:

$$\frac{\mathrm{D}\boldsymbol{\Omega}}{\mathrm{D}t} = -\underbrace{(\boldsymbol{\nabla}\cdot\boldsymbol{u})\,\boldsymbol{\Omega}}_{\text{gas expansion}} + \underbrace{(\boldsymbol{\Omega}\cdot\boldsymbol{\nabla})\,\boldsymbol{u}}_{\text{vortex stretching and bending}} + \underbrace{\frac{\boldsymbol{\nabla}\rho\times\boldsymbol{\nabla}p}{\rho^2}}_{\text{baroclinic torque}} + \underbrace{\boldsymbol{\nabla}\times\left(\frac{\boldsymbol{\nabla}\cdot\boldsymbol{\tau}}{\rho}\right)}_{\text{viscous diffusion}}. \quad (4.3)$$

Gas expansion reduces vorticity magnitudes, and consequently weakens the degree of interactions between the two shear layers. Therefore, it has a stabilizing effect on the system. In addition, vorticity is created through baroclinic torque, which also modifies the strength of the vorticity in the two shear layers. Moreover, the baroclinic mechanism is only active in regions with simultaneous pressure and density gradients; for the linearized analysis presented in the Appendix, this is due to the mean density gradient in the transverse direction interacting with the fluctuating pressure gradient in the axial direction. Small misalignments in the relative locations of the density and velocity gradients have a significant influence on baroclinic vorticity.

In reacting flows, this degree of misalignment between the time-averaged density and velocity gradients will be a strong function of the turbulent burning velocity, which controls the time-averaged speed at which the flame propagates into the unburned mixture and, thus, moves out of the velocity shear layer. For example, increasing laminar burning velocity or turbulence intensity will act to increase turbulent burning velocity and, hence, alter the relative locations of velocity and density gradients. The importance of this effect as a result of varying preheat temperature has been observed by Erickson & Soteriou (2011), who suggested that the resulting variations in wake structure that were observed were due in part to the flame moving away from the shear layer. This observation also suggests an explanation for why the transition in wake structure has been observed at different density ratio ranges in different experimental facilities. For example, wake transition has been observed within the density ratio range $3.2 \leqslant \rho_u/\rho_b \leqslant 5.6$ (Baudoin *et al.* 2009), $1.25 \leqslant \rho_u/\rho_b \leqslant 2.0$ (Erickson & Soteriou 2011), and $1.7 \leqslant \rho_u/\rho_b \leqslant 2.4$ for the current study. Each of these facilities has different operating conditions, fuels and Reynolds number conditions, and as a result is likely to have significantly different offsets between the density and shear layers. Even for a single backflow ratio, figure 17 shows the wide range of values that the stability limit could have in terms of density ratio, if the mean flame position moves only a tenth of the bluff-body diameter. In addition, with different bluff-body geometries, these facilities may have different maximum backflow ratios.

We next reinterpret the measured axial dependence of the centreline velocity fluctuations at $St_D = 0.24$ using the stability calculations. The axial coordinate is referenced to the location of maximum absolute growth rate, x_{AI} (obtained from figure 16), which for the simple top-hat profile corresponds to the location of maximum backflow ratio. These results are presented in figure 18.

Both plots show that, for a range of conditions, growth of the narrowband $St_D \sim 0.24$ fluctuations begins at approximately the same location, within roughly a half of the bluff-body diameter of one another, and that this location is centred near the numerically predicted peak in absolute growth rate at $x - x_{AI} \sim 0$. The analytical peak occurs slightly farther upstream, such that narrowband velocity fluctuations begin to grow at $(x - x_{AI})/D \sim -0.5$. Once the oscillations are initiated in the pocket of absolute instability, the structure associated with this mode continues to grow spatially as it passes through the downstream convectively unstable regime.

(a)

(b)

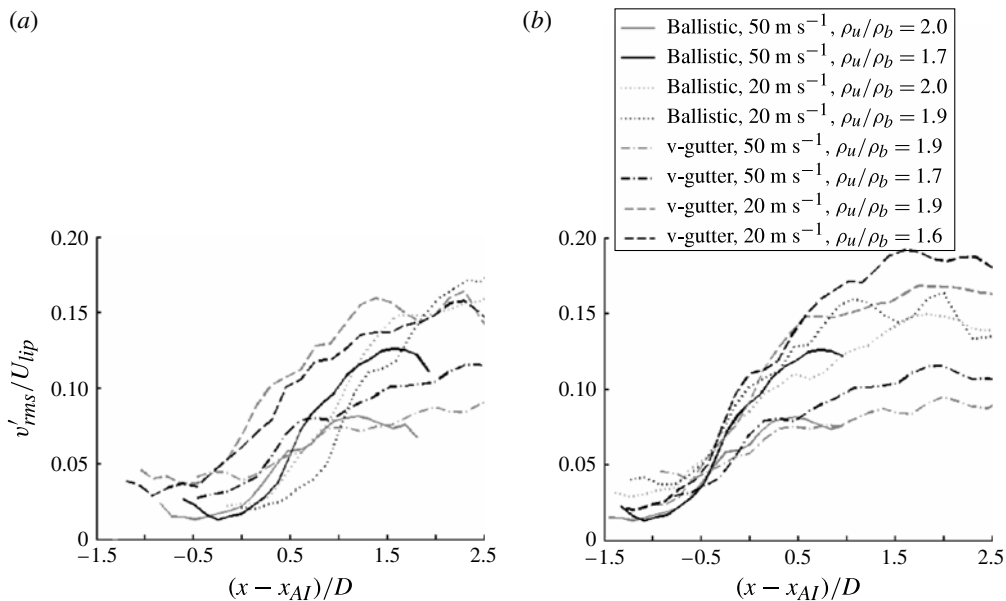|	Ballistic, 50 m s^{-1}, $\rho_u/\rho_b = 2.0$
	Ballistic, 50 m s^{-1}, $\rho_u/\rho_b = 1.7$
	Ballistic, 20 m s^{-1}, $\rho_u/\rho_b = 2.0$
	Ballistic, 20 m s^{-1}, $\rho_u/\rho_b = 1.9$
	v-gutter, 50 m s^{-1}, $\rho_u/\rho_b = 1.9$
	v-gutter, 50 m s^{-1}, $\rho_u/\rho_b = 1.7$
	v-gutter, 20 m s^{-1}, $\rho_u/\rho_b = 1.9$
	v-gutter, 20 m s^{-1}, $\rho_u/\rho_b = 1.6$

FIGURE 18. v'_{rms} at $St_D \sim 0.24$ versus distance downstream from the predicted location of maximum absolute growth rate for several test conditions showing: (*a*) numerical result from smoothed data; (*b*) analytical result from top-hat profiles.

It should be emphasized that the parallel stability analysis assumes a 'quiescent' base state, i.e. one without coherent or turbulent fluctuations. When the system is globally unstable, large vortices are alternately shed from the bluff body, which alter the time-averaged profiles. Therefore, while quantitative variations between this type of stability analysis and these data should be expected, the general agreement between model and data shown above illustrates that the key physical processes are nonetheless captured.

5. Intermittency

The spectral and correlation analysis section (§ 4.1) showed that there is a gradual increase in spectral energy at the asymmetric vortex shedding frequency as density ratio is decreased. In other words, the flow does not abruptly bifurcate to a globally unstable mode below some threshold density ratio. However, the measures of the flame and flow response illustrated above are averaged temporal attributes and do not illustrate that the flame dynamics are actually highly intermittent in time. As will be shown next, it appears that rather than characterizing the limit-cycle amplitude as monotonically growing in amplitude with ρ_u/ρ_b, a better description is that the flow has two possible states (a stable, noise-driven fixed point and a limit-cycling oscillation) and intermittently varies between them. This intermittency is an important finding of this work, as it suggests that the flow does not bifurcate suddenly when crossing the stability boundary; rather, the flow characteristics shift gradually due to intermittency as stability parameters are varied. The relative fraction of time the flow spends in each state monotonically varies with density ratio. This intermittent character is evident from figure 19, which shows a short sequence of flame images at the same operating condition; the flame has a generally symmetric structure at the beginning
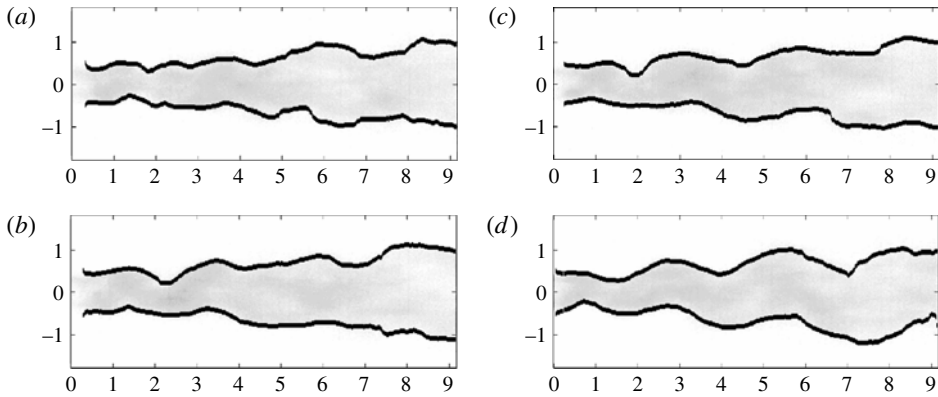
FIGURE 19. Sequence of flame images with edge tracking, demonstrating intermittent flame structure for ballistic bluff body at $U_{lip} = 50$ m s^{-1} and $\rho_u/\rho_b = 2.0$. (*a*) $t = 0$ ms; (*b*) $t = 1.33$ ms; (*c*) $t = 2.67$ ms; (*d*) $t = 4.00$ ms.
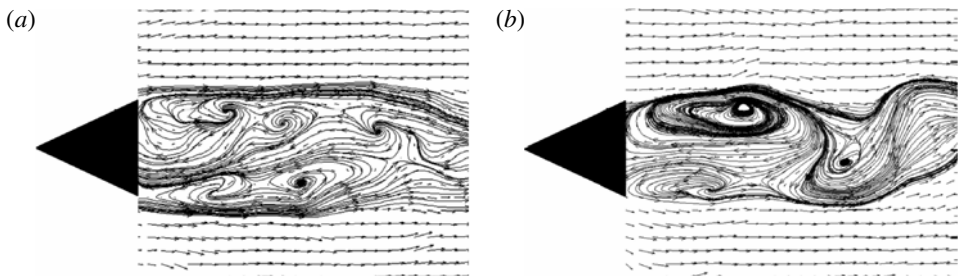

FIGURE 20. Instantaneous streamlines at two different times but the same operating condition for the v-gutter at $U_{lip} = 50$ m s^{-1}, $\rho_u/\rho_b = 2.0$, showing the intermittent character of the wake flow.

of the sequence, and has switched to a sinuous mode by the end. Additionally, figure 20 shows instantaneous streamlines calculated from PIV measurements at the same conditions. Figures 19 and 20 show the large-scale, asymmetric undulations of the flame/flow in some frames, with more disorganized features in other frames. The intermittent nature of the flame (and flow) is also apparent when observing the measured time signals from high-speed video (and PIV). For example, in time signals of flame edge motion (see figure 21), there are clearly periods of time where the signal is very noisy, but there are also periods of time when the signal appears to be nearly sinusoidal.

Indeed, analysis of various time windows of a given data set show that it erratically changes between random oscillations over a certain time interval, τ_n, to highly periodic oscillations over another time interval, τ_s. To quantify these observations, these intervals will be indexed such that $\tau_{n,j}$ represents the jth noisy event, and $\tau_{s,i}$ represents the ith sinusoidal event. Figure 21 illustrates these characteristic times using flame edge data. The duration of these two time intervals is a strong function of density ratio. Although these different behaviours appear erratically, they can be statistically characterized. As one method to quantify this intermittency, the time series were locally fitted to a sinusoidal fluctuation with a fixed frequency of $f_0 = 0.24U_{lip}/D$
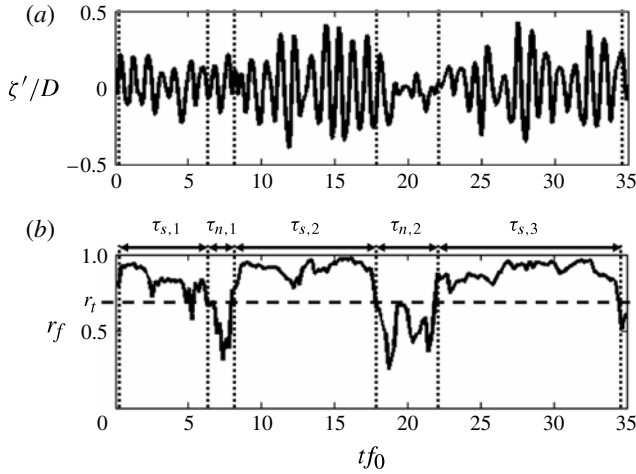
FIGURE 21. (*a*) Time signal of flame edge motion for $U_{lip} = 50\ \mathrm{m\ s^{-1}}$, $\rho_u/\rho_b = 2.0$, partitioned (and labelled accordingly) into sinusoidal times and noisy times; (*b*) r_f, defining when each time signal is approximately sinusoidal according to a threshold value, r_t.

over a two-period window, providing an amplitude $Z(x)$ and phase $\psi(x)$. Within each two-period window, a correlation coefficient, r_f, was calculated between the sine fit and the actual data, providing a measure of the goodness of fit:

$$r_f(x) = \frac{\langle \zeta_U(x,t)\, Z(x)\sin(2\pi f_0 t + \psi(x))\rangle}{\sqrt{\langle(\zeta_U(x,t))^2\rangle\,\langle(Z(x)\sin(2\pi f_0 t + \psi(x)))^2\rangle}}. \tag{5.1}$$

A sample plot of the temporal dependence of r_f at $\rho_u/\rho_b = 2.0$ is plotted in figure 21(*b*), illustrating that it spends a significant fraction of time between 0.8 and 1.0 for flame edge position (slightly less for the unsteady transverse velocity), but also has certain periods of time where it drops to values well below 0.5. In contrast, the results at $\rho_u/\rho_b = 2.4$ would show substantially more time with low correlation coefficients.

The fraction of time that this correlation coefficient exceeds a specified threshold value, r_t (shown on figure 21*b*), was computed at each spatial location and density ratio. Figure 22(*a*) plots a typical result at two threshold values, $r_t = 0.5$ and 0.8. Notice the similarities between the spectral energy plot, figure 14, and the intermittency plot, figure 22(*a*). Figure 22(*b*) shows a similar result plotted as a function of axial position for several density ratios.

These data clearly show that the rise in narrowband energy is associated with an increased fraction of time that the flow spends in a limit-cycling state, manifested by asymmetric structures with length scales of the order of the bluff-body diameter. However, the growth in amplitude with decreasing density ratio shown in figure 12 is not only due to intermittency effects, but also to a rise in limit-cycle amplitude during the time instants when the flow exhibits a highly periodic character. In order to quantify this point, we calculated the conditional amplitude of the sinusoidal fits averaged over the time intervals where $r_f > r_t$, denoted by $\zeta'_{rms}(r_f > r_t)$ in figure 23. The figure shows that the monotonic increase in narrowband spectral energy is not
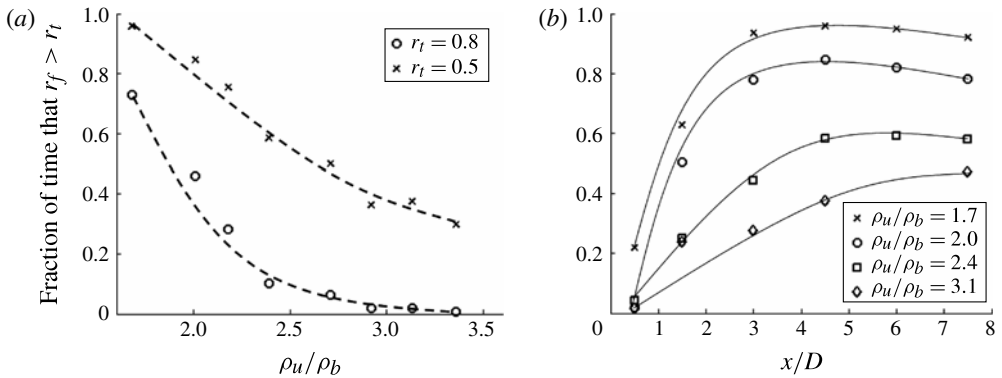
FIGURE 22. Fraction of time that upper flame edge sine-fit correlation coefficient is greater than the threshold value for the ballistic bluff body at $U_{lip} = 50$ m s^{-1}, plotted against: (a) density ratio at $x/D = 3.5$ and (b) axial position for $r_t = 0.8$.
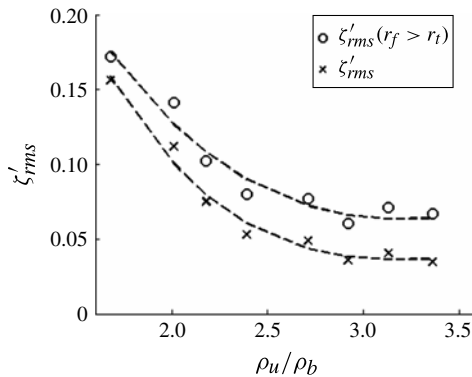

FIGURE 23. Effect of density ratio and intermittency on flame limit-cycle amplitude for the ballistic bluff body at $U_{lip} = 50$ m s^{-1}, $x/D = 3.5$.

only due to changes in intermittency characteristics, but also because of a rise in limit-cycle amplitude of the sinusoidal configuration as density ratio decreases.

As introduced previously, the time intervals of the 'sinusoidal' and 'random' bursts in the flame edge time series were determined, and were named τ_s and τ_n, respectively. These were obtained by traversing through the correlation coefficient time series (shown in figure 21b), and recording the time between crossings of the correlation coefficient threshold. Time spent above the threshold was associated with sinusoidal bursts, and time below the threshold was associated with random bursts. Thus, event durations were accumulated for both sinusoidal and random bursts. The probability density functions (p.d.f.s) of these event durations, τ_s and τ_n, very closely resemble exponential distributions, p.d.f.$(\tau > 0, \lambda) = \lambda e^{-\lambda \tau}$, where λ is a constant often referred to as the 'rate parameter'. Qualitatively, the p.d.f.s of τ_s reveal that as density ratio decreases, longer duration sinuous events become increasingly common (an increasingly large fraction of events have large τ_s). Although an exponential distribution provided the best fit to these p.d.f.s, τ_s and τ_n were also distributed very nearly log-normally. Log-normal behaviour of intermittent fluid phenomena is
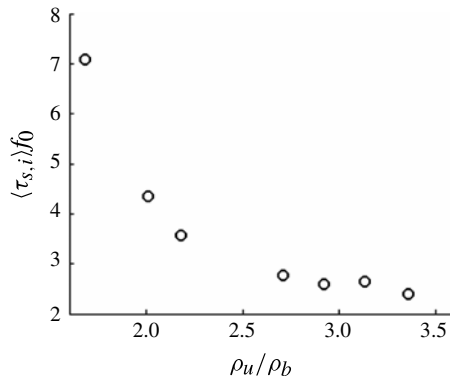
FIGURE 24. Density ratio dependence of $\langle\tau_{s,i}\rangle$ based on $\rho_t = 0.8$ and two-period shifting windows, at $x/D = 3.5$. Data are from the upper flame edge signal for the ballistic bluff body at $U_{lip} = 50$ m s^{-1}.
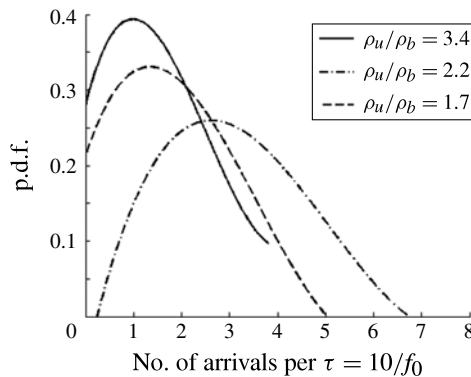

FIGURE 25. Smoothed distributions of the sinusoidal event arrival rate for several density ratios. Data are from the upper flame edge signal for the ballistic bluff body at $U_{lip} = 50$ m s^{-1}.

not uncommon; Kolmogorov (1962) suggested that the interval between intermittent 'bursts' in a turbulent boundary layer is distributed log-normally, a prediction that has also been experimentally observed (Rao, Narasimha & Badri Narayanan 1971). Likewise, turbulence intensity in atmospheric boundary layers is distributed log-normally (Kholmyansky, Moriconi & Tsinober 2007). Intermittency is also present in other aspects of bluff-body flows, such as Rai's (2010) observations of shear layer amplification rates.

The average durations of these 'sinusoidal' time intervals, $\langle\tau_{s,i}\rangle$, normalized by the limit-cycle period, are plotted against density ratio in figure 24 using a two-period window size. This result shows that $\langle\tau_{s,i}\rangle$ increases monotonically with decreasing density ratio. The figure shows that at the lowest density ratios, the average duration of the limit-cycling behaviour occupies as many as 7 periods of the oscillation, whereas at higher density ratios this behaviour persists, on average, for only 2 or 3 periods. This result shows that as density ratio is decreased, the sinuous, narrowband state becomes present for increased durations of time, i.e. the monotonic dependence on

density ratio shown in figure 22 is not due to an increased event rate, but an increased event duration. This becomes evident from figure 25, which presents the p.d.f.s of the event arrival rates; notice that the mean arrival rate first increases and then decreases as density ratio is decreased. In fact, the event rate for sinusoidal intervals becomes very low at low density ratios; this makes sense, because as density ratio decreases and the signal dwells in a sinusoidal configuration for much longer intervals, the event rate necessarily becomes low. The p.d.f.s shown in figure 25 correlate very well with a Poisson distribution.

Intermittent behaviours have been discussed extensively in nonlinear dynamical systems, and may arise from either deterministic or stochastic processes. Hilborn (1994) discusses several deterministic sources of intermittency, which include tangent bifurcation intermittency (Type I), Hopf-bifurcation intermittency (Type II), period-doubling intermittency (Type III), and on–off intermittency. For example, the Pomeau–Manneville scenario (Pomeau & Manneville 1980) is a deterministic route to chaos through intermittency; such an intermittency may be present even in a noiseless system.

Stochastic processes associated with either additive or parametric noise may also cause intermittency (Horsthemke & Lefever 1984). For example, consider a bi-stable dynamical system, such as a system in the vicinity of a subcritical bifurcation with a stable fixed point and limit cycle. In the presence of additive noise, the system may be bumped back and forth between the two stable solutions; the stationary probability density of such a system would have local maxima at values consistent with the locations of the potential wells. For example, Waugh & Juniper (2011) demonstrated this phenomenon in the context of the Rijke tube.

Parametric noise can also lead to intermittency in systems with supercritical bifurcations (Horsthemke & Lefever 1984). For example, consider a dynamical system with a single stable fixed point in the unforced system. Parametric noise can shift the stability boundary, as well as change the number or location of the maxima in the stationary probability density. A qualitative shift in the stationary p.d.f. is thus possible in the context of parametric noise.

The viscous, iso-density bluff-body wake undergoes a supercritical Hopf bifurcation at $Re_D \approx 35$ (White 2006). While we are not aware of theoretical studies that have explored the nature of this bifurcation for non-constant-density wakes, analysis of these data suggests that the bifurcation remains supercritical. For example, figure 26 plots the p.d.f. of the amplitude of the flame front oscillations, ζ', obtained from its Hilbert transform.

This figure does not show any behaviour indicative of multiple peaks in the amplitude p.d.f., which would be suggestive of a bi-stable system. Rather it shows a gradual shift in the peak amplitude to higher values as density ratio is reduced. Thus, these results suggest that the system undergoes a supercritical bifurcation in the presence of parametric background noise. An important remaining question, then, is what is the source of the parametric noise that leads to this intermittent behaviour? We will next show that this is due to random fluctuations in relative location of the shear layer and flame front. In the comparisons with local stability analysis section (§ 4.2), the large sensitivity of the flow stability to the degree of non-collocation between the density and shear layers was emphasized. Thus, relative motion of the shear layer and flame edge within the wave-maker region can lead to stochastic modulation of the global mode amplification rate. In order to illustrate this point, figure 27 plots a p.d.f. of the moving average (over a time interval of $3/f_0$) of the offset between the flame and the shear layer. The flame edge was obtained by edge-tracking the
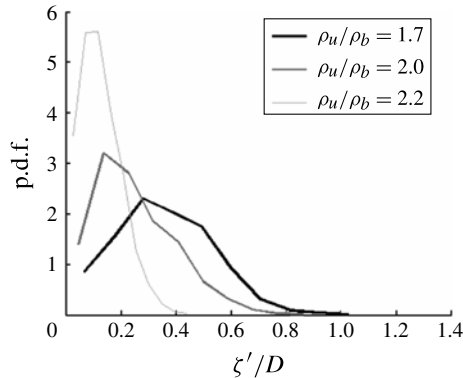
FIGURE 26. P.d.f. of the envelope of flame edge displacement, shown for several density ratios at $x/D = 4$.
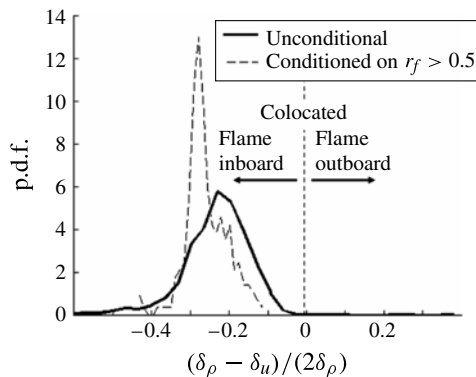

FIGURE 27. P.d.f. of the unconditioned and conditioned offset between the flame edge and the shear layer.

abrupt change in density in the Mie scattering images, and the shear layer point of inflection was obtained from the PIV measurement. The data for this plot were taken at $x/D = 2.0$, near the peak in absolute instability growth rate (see figure 16). Two p.d.f.s are presented, one unconditional, and the other conditioned on the value of $r_f > 0.5$ (indicative of periodicity of the flame measurement at the global mode frequency). At this axial position, the mean flame sits inboard of the shear layers (farther downstream, the mean flame propagates outboard of the shear layers). When a high degree of periodicity at the global mode frequency is observed, the flame is preferentially located even farther inboard, i.e. the peak in the p.d.f. of the conditioned offset is more than 50 % larger than the unconditioned value. Thus, the most probable offset between the flame and the shear layer is greater when periodic oscillations are observed than the most probable, unconditional offset between these layers.

We conclude this section by revisiting the local stability theory. As alluded to previously, such a comparison is complicated by the fact that no clearcut bifurcation in flow stability occurs. In order to compare the stability characteristics of the different geometries and velocities, figure 28 summarizes the data by plotting the maximum
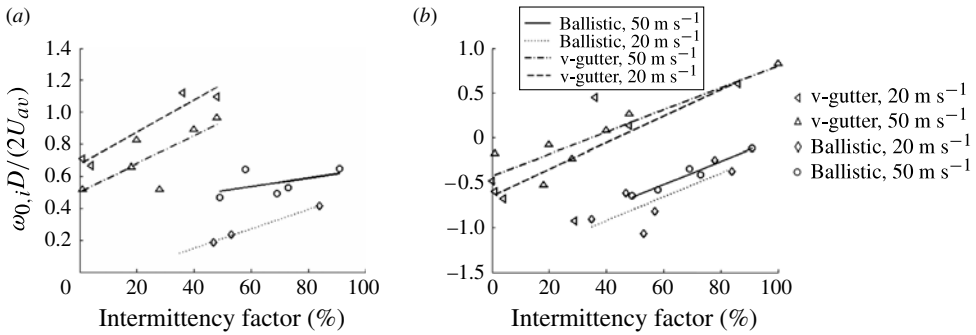
FIGURE 28. Dependence of predicted absolute growth rate upon measured intermittency factor, showing: (*a*) numerical result from smoothed data; (*b*) analytical result from top-hat profiles.

$\omega_{0,i}D/(2U_{av})$ for a given test (corresponding to the location of maximum reverse flow velocity) as a function of the intermittency factor. Intermittency is quantified by the fraction of time that $r_f > r_t = 0.5$. The figure shows that there is a good correlation between absolute growth rate and intermittency. Moreover, the slopes of all four data sets are comparable. It is also evident that predicted absolute growth rate values are systematically lower with the ballistic shape than the v-gutter (consistent with the lower backflow ratio for the ballistic shape).

These results show that the variation in intermittent characteristics of the flow is well correlated with the absolute stability characteristics of a quiescent base state flow with similar mean flow properties.

6. Concluding remarks

These results clearly show that the bluff-body wake structure is a strong function of density ratio and relative location of flame and velocity gradients. Results from parallel flow stability analysis were used to correlate various measured features of a reacting bluff-body wake. This information was used to show that the wake's large-scale sinuous motion, if it exists, is spawned at a location near the maximum absolute growth rate.

An important observation from this flow is that no sharp bifurcation occurs with variations in ρ_u/ρ_b. Rather, at intermediate density ratios the wake exhibits two behaviours intermittently. This intermittency is due to parametric noise associated with random fluctuations in relative offsets of the flame location and shear layer, which causes a stochastic modulation of the global mode growth rate. Additionally, this study shows that the wake mode intermittency is correlated with the maximum growth rate of absolute instability in the wake.

These results emphasize that the convective/absolute instability transition does not occur abruptly at a certain ρ_u/ρ_b value for the high-Reynolds-number flow considered here. This has significant implications for many important combustor applications which operate in the transitional, highly intermittent density range. This suggests that such flows intrinsically exhibit two co-existing dynamical states, intermittently jumping between the two. An important future study is to characterize the effects of narrowband acoustic excitation on these flow structures. While the effect of such
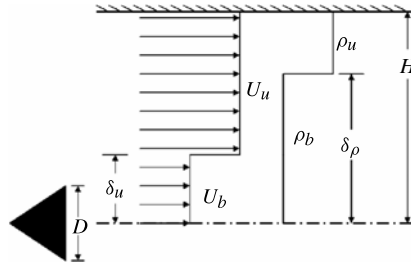
FIGURE 29. Geometry governing the dispersion relations in (A 1) and (A 3), for the sinuous wake mode with non-collocated density and shear layers.

excitation on a convectively or absolutely unstable flow is reasonably well understood (see § 1), its effects in this highly intermittent flow will require clarification.

Appendix

The dispersion relation for the confined, sinuous wake mode with non-collocated density and shear layers and rigid walls at $y = \pm H$, when the density layer is closer to the flow centreline than the shear layer, is

$$\frac{\rho_b}{\rho_u} \left\{ \frac{e^{k(\delta_\rho - \delta_u)} \left[1 + \alpha \dfrac{(U_u - c)^2}{(U_b - c)^2}\right] + e^{k(\delta_u - \delta_\rho)} \left[1 - \alpha \dfrac{(U_u - c)^2}{(U_b - c)^2}\right]}{e^{k(\delta_\rho - \delta_u)} \left[1 + \alpha \dfrac{(U_u - c)^2}{(U_b - c)^2}\right] - e^{k(\delta_u - \delta_\rho)} \left[1 - \alpha \dfrac{(U_u - c)^2}{(U_b - c)^2}\right]} \right\} = \frac{e^{k\delta_\rho} + e^{-k\delta_\rho}}{e^{k\delta_\rho} - e^{-k\delta_\rho}} \quad \text{(A 1)}$$

where c is modal wave phase speed, and α is a confinement parameter defined by

$$\alpha = \frac{e^{k\delta_u} + e^{2kH}e^{-k\delta_u}}{e^{k\delta_u} - e^{2kH}e^{-k\delta_u}}. \quad \text{(A 2)}$$

The dispersion relation for when the shear layer is closer to the flow centreline than the density layer is

$$\frac{(U_u - c)^2}{(U_b - c)^2} \left[\frac{\left(\dfrac{\rho_b}{\rho_u} + \alpha\right) e^{k(\delta_u - \delta_\rho)} - \left(\dfrac{\rho_b}{\rho_u} - \alpha\right) e^{k(\delta_\rho - \delta_u)}}{\left(\dfrac{\rho_b}{\rho_u} + \alpha\right) e^{k(\delta_u - \delta_\rho)} + \left(\dfrac{\rho_b}{\rho_u} - \alpha\right) e^{k(\delta_\rho - \delta_u)}} \right] = \frac{e^{k\delta_u} - e^{-k\delta_u}}{e^{k\delta_u} + e^{-k\delta_u}} \quad \text{(A 3)}$$

where α is defined by

$$\alpha = \frac{e^{k\delta_\rho} + e^{2kH}e^{-k\delta_\rho}}{e^{k\delta_\rho} - e^{2kH}e^{-k\delta_\rho}}. \quad \text{(A 4)}$$

The geometry used in these equations is provided in figure 29. This geometry was assumed symmetric about the bluff-body centreline, which is shown at the bottom of the figure. In the limiting case of $H \to \infty$ ($\alpha \to -1$) and $\delta_u = \delta_\rho$, these dispersion relations simplify to the unconfined result of Huerre & Monkewitz (1990) and Yu & Monkewitz (1990) as presented in § 1.

REFERENCES

ANDERSON, K. R., HERTZBERG, J. & MAHALINGAM, S. 1996 Classification of absolute and convective instabilities in premixed bluff body stabilized flames. *Combust. Sci. Technol.* **112** (1), 257–269.

ANSELMO-FILHO, P., HOCHGREB, S., BARLOW, R. S. & CANT, R. S. 2009 Experimental measurements of geometric properties of turbulent stratified flames. *Proc. Combust. Inst.* **32**, 1763–1770.

AQUARO, D. & PIEVE, M. 2007 High temperature heat exchangers for power plants: performance of advanced metallic recuperators. *Appl. Therm. Engng* **27** (2–3), 389–400.

BAUDOIN, E., YU, R., NOGENMYR, K. J., BAI, X. S. & FUREBY, C. 2009 Comparison of LES models applied to a bluff body stabilized flame. In *47th AIAA Aerospace Sciences Meeting Including the New Horizons Forum and Aerospace Exposition, Orlando, FL*. AIAA. AIAA-2009-1178.

BEARMAN, P. 1969 On vortex shedding from a circular cylinder in the critical Reynolds number regime. *J. Fluid Mech.* **37** (3), 577–585.

BEER, J. & CHIGIER, N. 1972 *Combustion Aerodynamics*. John Wiley and Sons.

BERS, A. 1983 *Handbook of Plasma Physics I: Basic Plasma Physics*. North-Holland.

BILL, R. G. JR. & TARABANIS, K. 1986 The effect of premixed combustion on the recirculation zone of circular cylinders. *Combust. Sci. Technol.* **47**, 39–53.

BLEVINS, R. D. 1977 *Flow-Induced Vibration*. Van Nostrand Reinhold Co.

BRIGGS, R. J. 1964 *Electron-stream Interaction with Plasmas*. MIT.

CANTWELL, B. & COLES, D. 1983 An experimental study of entrainment and transport in the turbulent near wake of a circular cylinder. *J. Fluid Mech.* **136**, 321–374.

CARDELL, G. S. 1993 Flow past a circular cylinder with a permeable wake splitter plate. PhD thesis, California Insititute of Technology, Pasadena.

CHAUDHURI, S. & CETEGEN, B. M. 2009 Response dynamics of bluff-body stabilized conical premixed turbulent flames with spatial mixture gradients. *Combust. Flame* **156** (3), 706–720.

CHAUDHURI, S., KOSTKA, S., RENFRO, M. W. & CETEGEN, B. M. 2010 Blowoff dynamics of bluff body stabilized turbulent premixed flames. *Combust. Flame* **157** (4), 790–802.

CRIMINALE, W. O., JACKSON, T. L. & JOSLIN, R. D. 2003 *Theory and Computation in Hydrodynamic Stability*. Cambridge University Press.

CROSS, C., FRICKER, A., SHCHERBIK, D., LUBARSKY, E., ZINN, B. T. & LOVETT, J. A. 2010 Dynamics of non-premixed bluff body-stabilized flames in heated air flow. In *ASME Turbo Expo, Glasgow, UK*. GT2010-23059.

CRUMP, J. E., SCHADOW, K. C., YANG, V. & CULICK, F. E. C. 1986 Longitudinal combustion instabilities in Ramjet engines: identification of acoustic modes. *J. Propul. Power* **2** (2), 105–109.

ERICKSON, R. R. & SOTERIOU, M. C. 2011 The influence of reactant temperature on the dynamics of bluff body stabilized premixed flames. *Combust. Flame* **158** (12), 2441–2457.

HERTZBERG, J. R., SHEPHERD, I. G. & TALBOT, L. 1991 Vortex shedding behind rod stabilized flames. *Combust. Flame* **86**, 1–11.

HILBORN, R. C. 1994 *Chaos and Nonlinear Dynamics*. Oxford University Press.

HO, C.-M. & HUERRE, P. 1984 *Perturbed Free Shear Layers*. University of Southern California.

HORSTHEMKE, W. & LEFEVER, R. 1984 *Noise Induced Transitions*. Springer.

HUANG, R. F. & CHANG, K. T. 2004 Oscillation frequency in wake of a vee gutter. *J. Propul. Power* **20** (5), 871–878.

HUERRE, P. & MONKEWITZ, P. A. 1985 Absolute and convective instabilities in free shear layers. *J. Fluid Mech.* **159**, 151–168.

HUERRE, P. & MONKEWITZ, P. A. 1990 Local and global instabilities in spatially developing flows. *Annu. Rev. Fluid Mech.* **22** (1), 473–537.

JUNIPER, M. P., TAMMISOLA, O. & LUNDELL, F. 2011 The local and global stability of confined planar wakes at intermediate Reynolds number. *J. Fluid Mech.* **686**, 218–238.

KARLOVITZ, B., DENNISTON, D. W., KNAPSCHAEFER, D. H. & WELLS, F. E. 1953 Studies on turbulent flames. *Proc. Combust. Inst.* **4**, 613–620.

KHOLMYANSKY, M., MORICONI, L. & TSINOBER, A. 2007 Large-scale intermittency in the atmospheric boundary layer. *Phys. Rev.* E **76** (2).

KIEL, B., GARWICK, K., LYNCH, A., GORD, J. R. & MEYER, T. 2006 Non-reacting and combusting flow investigation of bluff bodies in cross flow. In *42nd AIAA/ASME/SAE/ASEE Joint Propulsion Conference & Exhibit, Sacramento, California*. AIAA-2006-5234.

KIEL, B., GARWICK, K., LYNCH, A. & GORD, A. 2007 A detailed investigation of bluff body stabilized flames. In *45th AIAA Aerospace Sciences Meeting & Exhibit, Reno, Nevada*. AIAA-2007-168.

KIM, K. T. & HOCHGREB, S. 2011 The nonlinear heat release response of stratified lean-premixed flames to acoustic velocity oscillations. *Combust. Flame* **158**, 2482–2499.

KIM, W., LIENAU, J., VAN SLOOTEN, P., COLKET, M., MALECKI, R. & SYED, S. 2006 Towards modelling lean blowout in gas turbine flameholder applications. *Trans. ASME: J. Engng Gas Turbines Power* **128**, 40–48.

KOLMOGOROV, A. N. 1962 A refinement of previous hypotheses concerning the local structure of turbulence in a viscous incompressible fluid at high Reynolds number. *J. Fluid Mech.* **13** (1), 82–85.

LIEUWEN, T. C. & YANG, V. (ED.) 2005 Combustion instabilities in gas turbine engines: operational experience, fundamental mechanisms, and modeling. *Prog. Astronaut. Aeronaut.* **210**.

LOVETT, J. A., BROGAN, T. P., PHILIPPONA, D. S., KEIL, B. V. & THOMPSON, T. V. 2004 Development needs for advanced afterburner designs. *40th AIAA/ASME/SAE/ASEE Joint Propulsion Conference and Exhibit, Fort Lauderdale, FL*. AIAA-2004-4192.

MASSELIN, M. & HO, C.-M. 1985 Lock-on and instability in a flat plate wake. In *AIAA Shear Flow Control Conference, Boulder, CO*. AIAA-1985-571.

MEI, R. 1996 Velocity fidelity of flow tracer particles. *Exp. Fluids* **22**, 1–13.

MELLING, A. 1997 Tracer particles and seeding for particle image velocimetry. *Meas. Sci. Technol.* **8**, 1406–1416.

MONKEWITZ, P. A. 1988 The absolute and convective nature of instability in two-dimensional wakes at low Reynolds numbers. *Phys. Fluids* **31** (5).

NAIR, S. 2006 Acoustic detection of blowout phenomenon. PhD thesis, Georgia Institute of Technology, Atlanta, GA.

NAIR, S. & LIEUWEN, T. 2005 Acoustic detection of blowout in premixed flames. *J. Propul. Power* **21**, 32–39.

NICHOLS, J. W., SCHMID, P. J. & RILEY, J. J. 2007 Self-sustained oscillations in variable-density round jets. *J. Fluid Mech.* **582**, 341–376.

PAN, J. C., VANGSNESS, M. D. & BALLAL, D. R. 1992 Aerodynamics of bluff-body stabilized confined turbulent premixed flames. *Trans. ASME: J. Engng Gas Turbines Power* **114**, 783–789.

PERRY, A. E., CHONG, M. S. & LIM, T. T. 1982 The vortex shedding process behind two-dimensional bluff bodies. *J. Fluid Mech.* **116**, 77–90.

POINSOT, T. J., TROUVE, A. C., VEYNANTE, D. P., CANDEL, S. M. & ESPOSITO, E. J. 1987 Vortex-driven acoustically coupled combustion instabilities. *J. Fluid Mech.* **177**, 265–292.

POMEAU, Y. & MANNEVILLE, P. 1980 Intermittent transition to turbulence in dissipative dynamical systems. *Commun. Math. Phys.* **74**, 189–197.

POTTER, A. E. JR. & WONG, E. L. 1958 Effect of pressure and duct geometry on bluff-body flame stabilization. *National Advisory Committee on Aeronautics, Cleveland, OH*.

PRASAD, A. & WILLIAMSON, C. H. K. 1997 The instability of the shear layer separating from a bluff body. *J. Fluid Mech.* **333**, 375–402.

RAI, M. M. 2010 A computational investigation of the instability of the detached shear layers in the wake of a circular cylinder. *J. Fluid Mech.* **659**, 375–404.

RAO, K. N., NARASIMHA, R. & BADRI NARAYANAN, M. A. 1971 The 'bursting' phenomenon in a turbulent boundary layer. *J. Fluid Mech.* **48** (2), 339–352.

REES, S. J. 2009 Hydrodynamic instability of confined jets & wakes and implications for gas turbine fuel injectors. PhD thesis, University of Cambridge.

REES, S. J. & JUNIPER, M. 2010 The effect of confinement on the stability of viscous planar jets and wakes. *J. Fluid Mech.* **656**, 309–336.

ROSHKO, A. 1954 On the drag and shedding frequency of two-dimensional bluff bodies. *National Advisory Committee on Aeronautics.*

ROSHKO, A. 1955 On the wake and drag of bluff bodies. *J. Aeronaut. Sci.* **22** (2), 124–132.

ROSHKO, A. 1961 Experiments on the flow past a cylinder at very high Reynolds numbers. *J. Fluid Mech.* **10**, 345–356.

SCHLICHTING, H. & GERSTEN, K. 2000 *Boundary-Layer Theory.* Springer.

SCHMID, P. J. & HENNINGSON, D. S. 2001 *Stability and Transition in Shear Flows.* Springer.

SHANBHOGUE, S. 2008 Dynamics of perturbed exothermic bluff-body flow-fields. PhD thesis, School of Aerospace Engineering, Georgia Institute of Technology, Atlanta, GA.

SHANBHOGUE, S. J., HUSAIN, S. & LIEUWEN, T. 2009*a* Lean blowoff of bluff body stabilized flames: scaling and dynamics. *Prog. Energy Combust. Sci.* **35** (1), 98–120.

SHANBHOGUE, S. J., SHIN, D.-H., HEMCHANDRA, S., PLAKS, D. & LIEUWEN, T. 2009*b* Flame-sheet dynamics of bluff-body stabilized flames during longitudinal acoustic forcing. *Proc. Combust. Inst.* **32** (2), 1787–1794.

SMITH, D. A. & ZUKOSKI, E. E. 1985 Combustion instability sustained by unsteady vortex combustion. In *AIAA/SAE/ASME/ASEE Joint Propulsion Conference, Monterey, CA*. AIAA-1985-1248.

SOTERIOU, M. C. & GHONIEM, A. F. 1994 The vorticity dynamics of an exothermic, spatially developing, forced reacting shear layer. *Proc. Combust. Inst.* **25** (1), 1265–1272.

THURSTON, D. W. 1958 An experimental investigation of flame spreading from bluff body flameholders. Engineer's thesis, California Institute of Technology, Pasadena.

WAUGH, I. C. & JUNIPER, M. P. 2011 Triggering in a thermoacoustic system with stochastic noise. *Int. J. Spray Combust. Dyn.* **3** (3), 225–242.

WHITE, F. M. 2006 *Viscous Fluid Flow.* McGraw-Hill.

WILLIAMS, F. A. 1966 Flame stabilization of premixed turbulent gases. *Appl. Mech. Surveys* 1157–1170.

YAMAGUCHI, S., OHIWA, N. & HASEGAWA, T. 1985 Structure and blow-off mechanism of rod-stabilized premixed flame. *Combust. Flame* **62**, 31–41.

YANG, J. T., YEN, C. W. & TSAI, G. L. 1994 Flame stabilization in the wake flow behind a slit v-gutter. *Combust. Flame* **99**, 288–294.

YANG, V. & CULICK, F. E. C. 1986 Analysis of low frequency combustion instabilities in a laboratory Ramjet combustor. *Combust. Sci. Technol.* **45**, 1–25.

YU, M.-H. & MONKEWITZ, P. A. 1990 The effect of non-uniform density on the absolute instability of two-dimensional inertial jets and wakes. *Phys. Fluids* A **2** (7), 1175–1181.

ZDRAVKOVICH, M. M. 1997 *Flow Around Circular Cylinders: A Comprehensive Guide Through Flow Phenomena, Experiments, Applications, Mathematical Models, and Computer Simulations.* Oxford University Press.